Available online at www.sciencedirect.com
ScienceDirect
Comput. Methods Appl. Mech. Engrg. 385 (2021) 114019
Computer methods in applied mechanics and engineering
www.elsevier.com/locate/cma

Phase-field simulation of ductile fracture in shell structures

Davide Proserpio[a,b,*], Marreddy Ambati[c], Laura De Lorenzis[d], Josef Kiendl[a,b]

[a] Institute of Engineering Mechanics and Structural Analysis – Bundeswehr University Munich, Werner-Heisenberg-Weg 39, 85577 Neubiberg, Germany
[b] Department of Marine Technology – Norwegian University of Science and Technology, Otto Nielsens veg 10, 7052 Trondheim, Norway
[c] Institute of Solid Mechanics – TU Dresden, George-Bähr-Straße 3c, 01069 Dresden, Germany
[d] Department of Mechanical and Process Engineering – ETH Zürich, Tannenstraße 3, 8092 Zürich, Switzerland

Received 17 December 2020; received in revised form 24 June 2021; accepted 24 June 2021
Available online xxxx

Abstract

In this paper, a computational framework for simulating ductile fracture in multipatch shell structures is presented. A ductile fracture phase-field model at finite strains is combined with an isogeometric Kirchhoff–Love shell formulation. For the application to complex structures, we employ a penalty approach for imposing, at patch interfaces, displacement and rotational continuity and C^0 and C^1 continuity of the phase-field, the latter required if a higher-order phase-field formulation is adopted. We study the mesh dependency of the numerical model and we show that mesh refinement allows for capturing important features of ductile fracture such as cracking along shear bands. Therefore, we investigate the effectiveness of a predictor–corrector algorithm for adaptive mesh refinement based on LR NURBS. Thanks to the adoption of time- and space-adaptivity strategies, it is possible to simulate the failure of complex structures with a reasonable computational effort. Finally, we compare the predictions of the numerical model with experimental results.

Keywords: Phase-field model; Ductile fracture; Isogeometric; Shell; Multipatch; Adaptive refinement

1. Introduction

The numerical prediction of the fracture and post-failure behavior of shell structures constituted by ductile materials like metals requires sophisticated simulation tools. Adequate formulations for the description of ductility and fracture, in combination with structural models, are needed. The phase-field approach for the simulation of fracture has been the object of several studies in the last years. The formulation, stemming directly from Griffith's theory [1], is based on the description of brittle fracture in a variational framework presented by Francfort and Marigo [2], later regularized by Bourdin et al. [3]. The competition between the strain and the fracture surface energy controls the nucleation and growth of cracks, which are described by the smooth variation, between the intact and broken material states, of a continuous scalar parameter, the so-called phase-field. The formulation is now well established for the brittle fracture case thanks to various advances from the original formulation. Among

* Corresponding author at: Department of Marine Technology – Norwegian University of Science and Technology, Otto Nielsens veg 10, 7052 Trondheim, Norway.
E-mail address: davide.proserpio@ntnu.no (D. Proserpio).

https://doi.org/10.1016/j.cma.2021.114019

others, we recall the different approaches for introducing a split in the strain energy in order to take into account the physical asymmetry of the fracture behavior in tension and compression [4–7], for employing alternative degradation functions for the tensile part of the elastic strain energy instead of the standard quadratic one [8,9], for enforcing the irreversibility of fracture [5,10], and for adopting a higher-order phase-field formulation [11], or a dissipation function capable of reproducing the initial linear elastic behavior of the material before fracture [12].

The phase-field simulation of fracture in ductile materials requires a more complex formulation that includes, in addition to the elastic and fracture energy contributions already present in the brittle fracture approach, an energy dissipation term related to plastic deformation. The main challenge of these models is represented by the interaction between the dissipative term related to plasticity and the fracture term, and how these contributions are coupled, taking into account the fact that usually, in ductile materials, the plastic flow precedes the crack growth. Miehe et al. [13] consider a classical formulation of the fracture energy contributions (i.e. the same used for brittle fracture) applied to thermo-elastic–plastic materials and investigate the experimentally observed transition between brittle and ductile fracture due to dynamic loading conditions. The work by Alessi et al. [14] reviews several phase-field approaches for ductile fracture. The formulation proposed by Duda et al. [15] can be considered as a "brittle fracture in elasto-plastic solids" since no coupling is assumed between the phase-field and the plasticity. In the model by Ambati et al., at first proposed for the small strains framework [16] and then extended to finite strains [17], the coupling between the two terms is included in the degradation function of the tensile part of the elastic strain energy, since this function depends on the accumulated plastic strain. In the formulations by Alessi et al. [18,19], Borden et al. [9], Kuhn et al. [20], Huang et al. [21], Rodriguez et al. [22] and Miehe et al. [23], the damage-plastic coupling is based on the fact that a degradation function depending on the phase-field parameter is defined not only for the bulk elastic strain energy, but also for the hardening energy contribution and the plastic dissipated work. The latter two references include also a non-local gradient formulation for plasticity. The approach proposed by Yin and Kaliske [24] is based on the definition of the fracture toughness depending on the accumulated plastic deformation through the definition of a dedicated degradation function. Dittman and co-workers [25] adopt the higher-order phase-field formulation and couple the plasticity and fracture behaviors by degrading the critical fracture energy by a function depending on the equivalent plastic strain.

The phase-field method has been coupled with plate and shell models for simulating brittle fracture in thin-walled structures adopting different approaches [26–29]. The formulations by Kiendl et al. [30] and Paul et al. [31], based on the idea of performing the tension–compression split at various integration points through the shell thickness and then numerically integrating the strain energy contributions along these points, have been also extended to the case of multipatch structures with isogeometric analysis [32,33]. A similar approach has been recently adopted by Kikis et al. [34] for modeling phase-field brittle fracture in Reissner–Mindlin shells and plates. Pillai et al. [35] also presented a formulation for phase-field brittle fracture in a MITC4+ Reissner–Mindlin degenerated shell element. Formulations for ductile fracture have only been applied to a solid shell model in the small strains setting [36].

Several works are focused on the validation of the phase-field fracture approach through the comparison of the results of numerical simulations with experimental tests, such as [37–41] for the brittle case. For ductile fracture, we recall the works by Wick et al. [42] and Borden et al. [9] which report qualitative results for the fracture of screws and of a bolted plate, respectively. A quantitative comparison, showing good agreement of the results of ductile fracture phase-field simulations and experiments, is reported by Ambati et al. [17].

The aim of this work is to present an isogeometric phase-field approach for simulating the ductile fracture of thin plates and shells and to test and validate the model through the comparison of numerical analyses with experimental benchmarks. In addition, we study how the mesh refinement influences the results of the model in terms of fracture path and load–displacement curves. The computational efficiency of the simulations is therefore improved by employing a predictor–corrector algorithm for the adaptive local refinement of the mesh only in the region where it is needed, i.e. in the vicinity of the cracked area. In view of simulating the behavior of real-world structures, we adopt a penalty formulation for patch coupling that allows the description of geometrically complex multipatch structures.

The paper is outlined as follows. Section 2 provides the details of the proposed approach. Firstly, the elasto-plasticity formulation and its combination with a rotation-free isogeometric Kirchhoff–Love shell model are reviewed. A phase-field approach for ductile fracture at finite strains, including its higher-order formulation, is then presented and a detailed explanation is provided about its coupling to the elasto-plastic shell model. In the same section, we introduce the penalty formulation for coupling the structural and phase-field behaviors of adjacent

shells in multipatch structures and we briefly present the penalty contact formulation used for the simulation of the experimental tests. We also focus on the employed solution algorithm, especially on the staggering and on the adaptive step size schemes. Section 3 is devoted to the study of the effects of mesh refinement on the ductile fracture phase-field simulations through numerical experiments, and to the presentation and application of an adaptive local refinement procedure. In Section 4, the proposed approach is validated by the simulation and the comparison with the results of experimental tests performed on steel plates. The paper is closed by the conclusions in Section 5.

2. Formulation

This section presents the main features of the adopted phase-field ductile fracture approach and how this formulation is coupled with a model for shells and plates. Firstly, the main aspects of a Kirchhoff–Love shell formulation for elasto-plasticity are introduced, then a phase-field ductile fracture model valid in the finite strains regime is presented and combined with the structural model. Lastly, a penalty patch coupling and a penalty contact formulation, adopted for the numerical simulations of Section 4, are briefly recalled.

2.1. Elasto-plasticity formulation for Kirchhoff–Love shells

We adopt a rotation-free Kirchhoff–Love shell formulation developed by Kiendl et al. [43] in the framework of isogeometric analysis (IGA). The main assumption for thin shell theories is that segments which are perpendicular to the midsurface in the undeformed configuration remain straight and normal to the midsurface during deformation, so that the transverse shear deformation can be neglected. Therefore, the description of the shell kinematics is reduced to the description of its middle surface.

In the shell governing equations, we use the curvilinear coordinates θ^1 and θ^2 for the midsurface and the coordinate $\theta^3 \in [-t/2, +t/2]$ for the thickness direction, with t indicating the shell thickness. Considering a point $\mathbf{r}(\theta^1, \theta^2)$ on the middle surface of the shell, the tangent base vectors $\mathbf{a}_\alpha$, constituting a covariant coordinate system, are defined as:

$$\mathbf{a}_\alpha = \frac{\partial \mathbf{r}}{\partial \theta^\alpha}. \tag{1}$$

According to the adopted index notation, Greek indices α and β assume the values $\{1, 2\}$ for indicating the in-plane components, while Latin indices i and j take the values $\{1, 2, 3\}$. Partial derivatives with respect to θ^α are indicated as $(\cdot)_{,\alpha} = \partial(\cdot)/\partial\theta^\alpha$, so that Eq. (1) can be written also as $\mathbf{a}_\alpha = \mathbf{r}_{,\alpha}$. The dual contravariant base vectors are defined by $\mathbf{a}^\alpha \cdot \mathbf{a}_\beta = \delta^\alpha_\beta$, with δ^α_β being the Kronecker delta, and they can be used for defining a contravariant coordinate system on the shell midsurface. The unit normal vector in thickness direction is defined as:

$$\mathbf{a}_3 = \frac{\mathbf{a}_1 \times \mathbf{a}_2}{\|\mathbf{a}_1 \times \mathbf{a}_2\|}. \tag{2}$$

Considering a point in the shell continuum and $\mathbf{x}$ being its position vector in the deformed configuration, the position of the vector can be described, due to the Kirchhoff assumption, by the corresponding point on the midsurface $\mathbf{r}$ and the fiber director $\mathbf{a}_3$:

$$\mathbf{x} = \mathbf{r} + \theta^3 \mathbf{a}_3. \tag{3}$$

Accordingly, the base vectors, defined at any point $\mathbf{x}$ in the shell continuum, are denoted as $\mathbf{g}_i = \mathbf{x}_{,i}$ and take the form:

$$\mathbf{g}_\alpha = \mathbf{a}_\alpha + \theta^3 \mathbf{a}_{3,\alpha}, \qquad \mathbf{g}_3 = \mathbf{a}_3. \tag{4}$$

The dual contravariant base vectors can be retrieved by the expression $\mathbf{g}^i \cdot \mathbf{g}_j = \delta^i_j$. As follows, the notation $\mathring{(\cdot)}$ indicates the undeformed configuration of the geometric variables. With these terms in hand, the covariant components of the deformation gradient $\mathbf{F} = d\mathbf{x}/d\mathring{\mathbf{x}}$, in the curvilinear reference system constituted by the contravariant bases in the undeformed configuration $\mathring{\mathbf{g}}^i \otimes \mathring{\mathbf{g}}^j$, can be computed as:

$$F_{ij} = \mathring{\mathbf{g}}_i \cdot \mathbf{g}_j. \tag{5}$$

Accordingly, the right Cauchy–Green deformation tensor $\mathbf{C} = \mathbf{F}^T\mathbf{F}$ covariant components can be defined as:

$$C_{ij} = \mathbf{g}_i \cdot \mathbf{g}_j. \tag{6}$$

The adopted approach for plasticity, based on the work from Simo [44], consists in a standard three-dimensional isochoric von-Mises J_2 rate-independent plasticity theory at finite strains, which employs a multiplicative decomposition of the deformation gradient into its elastic and plastic parts:

$$\mathbf{F} = \mathbf{F}^e \mathbf{F}^p. \tag{7}$$

From the elastic deformation gradient, the elastic left Cauchy–Green deformation tensor $\mathbf{b}^e$ is computed as:

$$\mathbf{b}^e = \mathbf{F}^e \mathbf{F}^{eT}. \tag{8}$$

The determinant of the elastic deformation gradient tensor, which is a measure of the elastic change of volume, is designated as $J^e = \det[\mathbf{F}^e]$. We adopt a neo-Hookean constitutive law of decoupled type for describing the elastic behavior of the material. According to this approach, the strain energy density ψ_e can be additively decomposed into a volumetric (shape preserving) and a deviatoric (volume preserving) part:

$$\psi_e = \psi_e^{vol} + \psi_e^{dev}. \tag{9}$$

The two terms are computed as follows:

$$\psi_e^{vol} = \frac{\kappa_0}{2}\left(\frac{J^{e2}-1}{2} - \ln J^e\right), \tag{10}$$

$$\psi_e^{dev} = \frac{\mu}{2}\left(\bar{I}_b^e - 3\right), \tag{11}$$

with κ_0 and μ as the bulk and shear modulus of the material, respectively. In Eq. (11), $\bar{I}_b^e = \mathrm{tr}[\bar{\mathbf{b}}^e]$, with $\bar{\mathbf{b}}^e = J^{e-\frac{2}{3}}\mathbf{b}^e$. Further details regarding the plasticity model, including the formulation of the yield function, the associative flow rule, and the time-integration scheme required for the solution of the elasto-plastic constitutive equations, can be found in Ambati et al. [45].

For the implementation of the elasto-plasticity model in the shell formulation, we adopt a stress-based approach consisting in defining integration points in the shell thickness direction where the validity of the three-dimensional material model is enforced. Consequently, the stress resultants are computed by the integration of the stress components through the thickness. In the finite strain context, it is important to point out that the considered shell formulation defines only the midsurface deformation, while the thickness deformation is neglected. In order to take into account the out-of-plane deformation, we follow the same approach as in Kiendl et al. [46] and Ambati et al. [45], and we correct the definition of the base vector in thickness direction:

$$\mathbf{g}_3 = \lambda_3 \mathbf{a}_3, \tag{12}$$

where λ_3 is the thickness stretch. Accordingly, the change of $\mathbf{g}_3$ modifies the definition of the components of the deformation gradient:

$$F_{i\beta} = \mathring{\mathbf{g}}_i \cdot \mathbf{g}_\beta, \qquad F_{i3} = \lambda_3\, \mathring{\mathbf{g}}_i \cdot \mathbf{a}_3, \tag{13}$$

and also of the Cauchy–Green deformation tensor:

$$C_{\alpha\beta} = \mathbf{g}_{\alpha\beta}, \qquad C_{\alpha 3} = 0, \qquad C_{33} = {\lambda_3}^2. \tag{14}$$

However, the information about the thickness deformation cannot be retrieved directly from the shell kinematics, which is based only on the displacement field of the midsurface. For this purpose, we employ the plane stress condition as an additional constraint. This condition is expressed by the contravariant component $S^{33} = 0$ of the second Piola–Kirchhoff stress tensor $\mathbf{S} = S^{ij}\mathring{\mathbf{g}}_i \otimes \mathring{\mathbf{g}}_j$. According to the considered approach, the plane stress condition is enforced locally, in an iterative manner, at each thickness integration point. Without entering into the details, which can be found in [45], the process starts by choosing the value of λ_3 from the last converged load step ($\lambda_3 = 1$ for the first step), then the deformation gradient tensor is corrected as in Eq. (13) and the updated Cauchy–Green deformation tensor is computed as $\mathbf{C} = \mathbf{F}^T\mathbf{F}$. From the corrected $\mathbf{F}$, the stress tensor $\mathbf{S}$ and the elasto-plastic material tangent tensor $\mathbb{C}$ are computed according to J_2 plasticity theory [44]. With these quantities in hand, the linearization of the plane stress conditions allows us to compute an updated value of C_{33} from the just obtained S^{33} and $\mathbb{C}^{3333}$. According to Eq. (14), the updated value of the thickness stretch is easily found as:

$$\lambda_3 = \sqrt{C_{33}}. \tag{15}$$

This value is used for obtaining again the corrected deformation gradient and Cauchy–Green deformation tensors, as in Eqs. (13) and (14). From this point, the iterative process starts again and it is repeated until the plane stress condition is satisfied within a specific tolerance. With this procedure, the stress resultants and the material tensor can be computed at any point of the continuum, specifically in the considered thickness integration point. The strain tensor $\boldsymbol{\varepsilon}$, according to the Kirchhoff–Love formulation, can be defined at any location of the shell, based on the midsurface kinematics, as the sum of the membrane and bending parts as follows:

$$\boldsymbol{\varepsilon}(\theta^3) = \boldsymbol{\varepsilon}^m + \theta^3 \boldsymbol{\kappa}, \tag{16}$$

where $\boldsymbol{\varepsilon}^m = \varepsilon^m_{\alpha\beta}\, \mathbf{a}^\alpha \otimes \mathbf{a}^\beta$ is the membrane strain tensor, whose covariant components can be expressed as:

$$\varepsilon^m_{\alpha\beta} = \frac{1}{2}\left(\mathbf{a}_\alpha \cdot \mathbf{a}_\beta - \mathring{\mathbf{a}}_\alpha \cdot \mathring{\mathbf{a}}_\beta\right). \tag{17}$$

The second term in Eq. (16) is related to bending and varies linearly with the thickness coordinate θ^3. The covariant components of the curvature change tensor $\boldsymbol{\kappa} = \kappa_{\alpha\beta}\, \mathbf{a}^\alpha \otimes \mathbf{a}^\beta$ are computed as:

$$\kappa_{\alpha\beta} = \mathring{\mathbf{a}}_{\alpha,\beta} \cdot \mathring{\mathbf{a}}_3 - \mathbf{a}_{\alpha,\beta} \cdot \mathbf{a}_3. \tag{18}$$

The presence of the second-order derivatives in the curvature expression in Eq. (18) requires at least C^1 continuity of the shape functions of the discretized model, making IGA a favorable choice for the discretization of the thin shell formulation.

The variational formulation used for the discretized model is based on the virtual work principle and corresponds to the weak form of the momentum equation:

$$\delta W = \delta W^{\text{int}} - \delta W^{\text{ext}} = 0. \tag{19}$$

In the definition of the internal virtual work:

$$\delta W^{\text{int}} = \int_A \left(\delta \boldsymbol{\varepsilon}^m : \boldsymbol{n} + \delta \boldsymbol{\kappa} : \boldsymbol{m}\right) dA, \tag{20}$$

$\delta \boldsymbol{\varepsilon}^m$ and $\delta \boldsymbol{\kappa}$ are computed according to Eqs. (17), (18) and related ones, considering a virtual displacement field $\delta \mathbf{u}$. The effective stress resultants $\boldsymbol{n}$ and $\boldsymbol{m}$, for axial force and bending respectively, are computed employing numerical integration of the stresses through the thickness.

2.2. Higher order phase-field model for ductile fracture

In the phase-field fracture model, the nucleation and/or evolution of cracks are solely described through the minimization of an energy functional, as first proposed, for the case of brittle fracture, by Bourdin et al. [3]. For the ductile fracture case, we assume a regularized energy functional that includes elastic, plastic and fracture energy contributions, as in Ambati et al. [16,17]:

$$E_\ell(\bar{\mathbf{b}}^e, J^e, \alpha, s) = \int_\Omega \left[\psi_e(\bar{\mathbf{b}}^e, J^e, p, s) + \psi_p(\alpha) + \psi_s(s)\right] dV. \tag{21}$$

The term $\psi_p(\alpha)$ represents the plastic strain energy density function, under the assumption of isotropic hardening, and α is the relative internal hardening variable corresponding to the equivalent accumulated plastic strain.

The fracture energy density function ψ_s, introduced by Bourdin et al. [3] in the regularized formulation of brittle fracture, can be expressed in its original form ("second-order phase-field model"):

$$\psi_{s,2}(s, \nabla s) = G_c \left[\frac{(1-s)^2}{4\ell} + \ell |\nabla s|^2\right], \tag{22}$$

or in the so-called "fourth-order phase-field model" form, as proposed by Borden et al. [11]:

$$\psi_{s,4}(s, \nabla s, \Delta s) = G_c \left[\frac{(1-s)^2}{4\ell} + \frac{\ell}{2}|\nabla s|^2 + \frac{\ell^3}{4}(\Delta s)^2\right]. \tag{23}$$

Choosing an expression of the fracture energy density as in Eq. (23) would lead to a higher-order formulation of the phase-field ductile fracture model, that has shown superior convergence rate with respect to the standard formulation [11,32] and therefore will be adopted, whenever possible, in the numerical simulations present in this

paper. As for the Kirchhoff–Love shell formulation, a discretization employing isogeometric analysis can provide the continuity required by the higher order derivatives present in the fourth-order model (C^1 continuity). For both formulations, ψ_s depends on the phase-field scalar variable s, whose smooth transition from 1, corresponding to intact material, to 0, corresponding to fully broken material, approximates the crack topology in the considered domain Ω. The scalar term ℓ is a length scale parameter that controls the width of the transition zone of the phase-field and G_c represents the fracture toughness of the material. Eqs. (22) and (23) employ a quadratic dissipation function in the form $(1-s)^2$, following the so-called "AT2 model" originally proposed by Ambrosio and Tortorelli [47] and later adopted by Bourdin et al. [3]. This formulation leads to a material model that does not show a perfectly linear elastic behavior, since the damage starts to accumulate from the beginning of the analysis. An alternative is represented by the "AT1 model", proposed by Pham et al. [12], which employs a linear dissipation function $(1-s)$ and according to which a linear elastic behavior of the material is obtained.

Intending to distinguish the different fracture behaviors of the material in tension and compression, we adopt an additive decomposition of the elastic strain energy ψ_e in its positive (tensile and shear, ψ_e^+) and negative (compressive, ψ_e^-) parts. Following the model adopted for the description of the J_2 plasticity, the decomposition involves the volumetric and deviatoric contributions of the strain energy (see Eqs. (10) and (11)), as in Borden et al. [9] (whose approach is based on the split, introduced in the small strains framework, by Amor et al. [4]), so that:

$$\begin{aligned} J^e < 1 \begin{cases} \psi_e^+ = \psi_e^{dev}(\bar{\mathbf{b}}^e) \\ \psi_e^- = \psi_e^{vol}(J^e) \end{cases} \\ J^e \geq 1 \begin{cases} \psi_e^+ = \psi_e^{dev}(\bar{\mathbf{b}}^e) + \psi_e^{vol}(J^e) \\ \psi_e^- = 0 \end{cases} \end{aligned} \tag{24}$$

Accordingly, only the positive part of the elastic strain energy is degraded by the degradation function $g(s, p)$:

$$\psi_e(\bar{\mathbf{b}}^e, J^e, p, s) = g(s, p)\, \psi_e^+(\bar{\mathbf{b}}^e, J^e) + \psi_e^-(J^e). \tag{25}$$

The degradation function, which accounts for the deterioration of the material due to the nucleation and growth of microcracks, includes a positive small factor $\eta \approx 0$ for avoiding zero stiffness of the material in the fully cracked state, and takes the form:

$$g(s, p) = (1-\eta)s^{2p^m} + \eta, \tag{26}$$

with

$$p = \frac{\alpha}{\alpha_{crit}}. \tag{27}$$

In Eq. (26), the presence of p, which describes the localization and accumulation of the plastic strains, couples the plastic behavior of the material with the fracture process. The phase-field is dependent on the accumulation of the ductile damage, as the fracture can develop only in regions with significant (i.e. comparable with the critical value of the hardening variable α_{crit}) plastic strains. For elasto-plastic materials, this is in agreement with the observation that fracture occurs in areas that undergo high plastic strain. Additionally, the present formulation implies that, once the fracture starts evolving in a certain region, the plastic strain ceases to accumulate, so that the occurring deformations are totally elastic in that area. It is important to point out that, for $\alpha = \alpha_{crit}$, the standard quadratic degradation function is retrieved. The parameters α_{crit} and m can be considered as material parameters that need to be calibrated through the comparison with experimental results. The second one can assume the values $m = \{1, 2, 3, \ldots\}$ and controls the speed of the ductile fracture process. A higher value of m allows for a slower accumulation of the damage when $p < 1$, i.e. $\alpha < \alpha_{crit}$, and for a faster accumulation when the hardening values exceeds the critical threshold [16].

The stationarity condition of the energy functional in Eq. (21) with respect to s leads to the strong form of the phase-field evolution equation for ductile fracture which reads, for the second- and fourth-order formulations respectively,

$$\frac{2\,\ell}{G_c} g_{,s} \psi_e^+ + s - 4\,\ell^2 \Delta s = 1, \tag{28}$$

$$\frac{2\,\ell}{G_c} g_{,s} \psi_e^+ + s - 2\,\ell^2 \Delta s + \ell^4 \Delta(\Delta s) = 1, \tag{29}$$

where:

$$g_{,s} = \frac{\partial g(s,\, p)}{\partial s} = (1-\eta) 2 p^m s^{(2p^m-1)}. \tag{30}$$

Unlike for the brittle fracture model, in this case, the phase-field evolution equation is nonlinear.

The irreversibility of the fracture, meaning that cracks will not heal if the external loads are removed, is enforced by introducing in the phase-field model the following local history variable $\mathcal{H}^e$, defined as the maximum of the positive part of the elastic strain energy density up to the current pseudo-time T:

$$\mathcal{H}^e(T) := \max_{\tau \in [0,T]} \psi_e^+(\bar{\mathbf{b}}^e,\, J^e,\, \tau). \tag{31}$$

The history variable replaces ψ_e^+ in the phase-field evolution equation.

2.3. Phase-field ductile fracture modeling for thin shells and plates

The combination of the ductile fracture phase-field approach with the considered Kirchhoff–Love shell model is based on the methodology adopted by Kiendl et al. [30] for the brittle fracture case, which can be employed regardless of the specific shell formulation. Accordingly, the model is reduced to the behavior of the midsurface variables and we introduce the strain energy surface density Ψ_e, which expresses the elastic strain energy per unit area of the midsurface:

$$\Psi_e = \int_{-t/2}^{+t/2} \psi_e(\theta^3)\, d\theta^3. \tag{32}$$

Analogously, we can define the fracture energy surface density $\Psi_s(s)$, from the through-thickness integration of ψ_s, and the plastic energy surface density $\Psi_p(\alpha)$, based on the integration of $\psi_p(\alpha)$ along the thickness. Consequently, for the case of plates or shells, the energy functional in Eq. (21) can be rewritten in the following form:

$$E_\ell(\bar{\mathbf{b}}^e,\, J^e,\, \alpha,\, s) = \int_A \left[\, \Psi_e(\bar{\mathbf{b}}^e,\, J^e,\, s,\, p) + \Psi_p(\alpha) + \Psi_s(s) \right] dA. \tag{33}$$

Fig. 1 shows how, due to the bending component related to the shell curvature change, the strain tensor linearly varies from tension to compression through the thickness (see also Eq. (16)). Moreover, as a consequence of the assumed plastic behavior of the material and of the degradation of the tensile part of the stress tensor due to the phase-field fracture formulation, the stress tensor itself can have a nonlinear distribution along the shell thickness. For this reason, numerical integration is employed for computing the integral in Eq. (32) and special attention is required for the tension–compression split, which is operated according to Eq. (24) at each thickness integration point. Since the correct strain tensor depends both on the membrane and on the bending components, the split needs to be computed on the total strain energy without separating the membrane and bending parts.

Unlike the formulation for brittle fracture, the adopted degradation function (see Eq. (26)) depends not only on the phase-field variable s, but also on the plasticity-related scalar parameter p that, according to the definition in Eq. (27), depends on the hardening parameter α. Since α can vary through the shell thickness, also the degradation function varies through the thickness. So, in this approach, we assume the phase-field parameter, which is defined only on the midsurface, to be constant through the thickness, but we obtain a non-constant degradation function and nonlinear distributions of the stresses (see again Fig. 1). This means that, when the integral in Eq. (32) is computed taking into account the tension–compression split,

$$\Psi_e = \int_{-t/2}^{+t/2} \left[g(s,\, p) \psi_e^+(\bar{\mathbf{b}}^e,\, J^e) + \psi_e^-(J^e) \right] d\theta^3, \tag{34}$$

the degradation function term $g(s,\, p)$ needs to be included in the through-thickness numerical integration. As a consequence, the strong form of the phase-field ductile fracture evolution equation for shells, based on the stationarity condition of the energy functional (33) with respect to s, is:

$$\frac{2\,\ell}{t G_c} \int_t g_{,s} \psi_e^+\, d\theta^3 + s - 4\,\ell^2 \Delta s = 1, \tag{35}$$

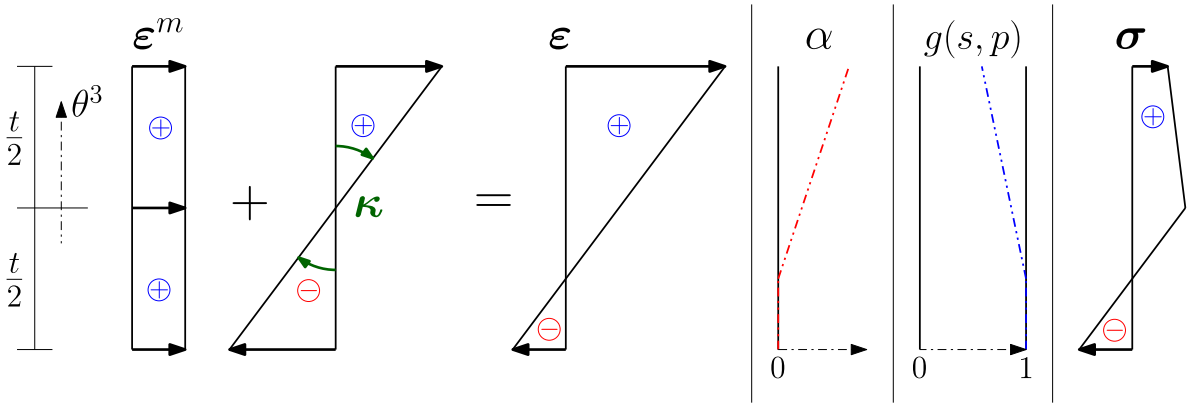

Fig. 1. Combination of the contributions of membrane and bending strain and total strain $\boldsymbol{\varepsilon}$ over the thickness t for a shell subjected to bending and tension. Possible distributions of the hardening variable α and of the degradation function $g(s,p)$ along t. As a result, the through-thickness stress $\boldsymbol{\sigma}$ distribution after degradation of the positive (tensile) component is depicted.

$$\frac{2\,\ell}{t G_c}\int_t g_{,s}\psi_e^+\,d\theta^3 + s - 2\,\ell^2\Delta s + \ell^4\Delta(\Delta s) = 1, \tag{36}$$

with Eq. (35) valid for the second-order formulation and (36) for the higher-order model. The weak form of the two previous equations, including δs as a test function and considering the usual boundary conditions of the phase-field problem, read:

$$\int_A\left(\frac{2\,\ell}{t G_c}\int_t g_{,s}\mathcal{H}^e d\theta^3 + s - 1\right)\delta s\;dA + 4\,\ell^2\int_A \nabla s\cdot\nabla\delta s\;dA = 0, \tag{37}$$

$$\int_A\left(\frac{2\,\ell}{t G_c}\int_t g_{,s}\mathcal{H}^e d\theta^3 + s - 1\right)\delta s\;dA + 2\,\ell^2\int_A \nabla s\cdot\nabla\delta s\;dA + \ell^4\int_A \Delta s\cdot\Delta\delta s\;dA = 0. \tag{38}$$

The previous equations employ the history field $\mathcal{H}^e$ for enforcing the irreversibility of the fracture and need to be solved by an iterative solver due to their nonlinearity. In the discretized framework, the variation of the expressions (37) and (38) with respect to the discrete value of the phase-field at the control points s_r leads to the expression of the residual phase-field vector $\mathbf{R}_{PF}$, whose linearization yields the tangent stiffness matrix $\mathbf{K}_{PF}$. So, the linearized version of the phase-field evolution equation, which is solved for an increment of the vector of the discrete phase-field values at control points $\Delta\mathbf{s}$, simply becomes:

$$\mathbf{K}_{PF}\;\Delta\mathbf{s} = \mathbf{R}_{PF}. \tag{39}$$

2.4. Penalty-based coupling of adjacent shell patches

In view of simulating the fracture behavior of complex multipatch shell structures, as done in Section 4.2, a penalty-based approach for coupling adjacent isogeometric patches is adopted. Both the structural and the phase-field behaviors across the patch interfaces are coupled and a single dimensionless penalty term $\alpha_{glob} = 10^3$, scaled by the problem parameters, is needed for all the coupling terms.

Considering two patches A and B that share an interface curve $\mathcal{L}$, the structural coupling consists in imposing displacement and rotational continuity across the patch connection by augmenting the virtual work formulation in Eq. (19) by adding the terms δW^{pd} and δW^{pr}. The first term imposes the displacement continuity:

$$\delta W^{\mathrm{pd}} = \int_{\mathcal{L}}\alpha_{\mathrm{d}}\left(\mathbf{u}^A - \mathbf{u}^B\right)\cdot\left(\delta\mathbf{u}^A - \delta\mathbf{u}^B\right)d\mathcal{L}, \tag{40}$$

while the second one preserves the rotational continuity:

$$\begin{aligned}\delta W^{\mathrm{pr}} = \int_{\mathcal{L}}\alpha_{\mathrm{r}}\Big(&\left(\mathbf{a}_3^A\cdot\mathbf{a}_3^B - \mathring{\mathbf{a}}_3^A\cdot\mathring{\mathbf{a}}_3^B\right)\left(\delta\mathbf{a}_3^A\cdot\delta\mathbf{a}_3^B - \delta\mathring{\mathbf{a}}_3^A\cdot\delta\mathring{\mathbf{a}}_3^B\right) + \\ &+ \left(\mathbf{a}_n^A\cdot\mathbf{a}_3^B - \mathring{\mathbf{a}}_n^A\cdot\mathring{\mathbf{a}}_3^B\right)\left(\delta\mathbf{a}_n^A\cdot\delta\mathbf{a}_3^B - \delta\mathring{\mathbf{a}}_n^A\cdot\delta\mathring{\mathbf{a}}_3^B\right)\Big)\,d\mathcal{L},\end{aligned} \tag{41}$$

where $\mathbf{a}_n^A$ is the unit vector lying in the plane of patch A and perpendicular to $\mathcal{L}$. For further details regarding the formulation, the reader is referred to the work by Herrema et al. [48], according to which the penalty terms α_{d} and α_{r} are computed by scaling the global penalty parameter $\alpha_{glob} = 10^3$ with the membrane and bending elastic stiffness values of the coupled shells. In our case, uniform isotropic materials are considered, so:

$$\alpha_{\mathrm{d}} = g(s,\, p)\, \alpha_{glob} \frac{E\, t}{h\,(1-\nu^2)}, \tag{42}$$

$$\alpha_{\mathrm{r}} = g(s,\, p)\, \alpha_{glob} \frac{E\, t^3}{12\, h\,(1-\nu^2)}, \tag{43}$$

with E as the Young's modulus, ν as the Poisson's ratio, and t as the shell thickness, while h is the average element length along the coupled edge having the finer discretization. The meaning of h needs to be specified, since the formulation can handle non-conforming meshes at the two sides of the coupled edge, thus it can be used in combination with adaptive mesh refinement technologies. The phase-field degradation function $g(s,\, p)$ ensures a consistent scaling between the structural and penalty stiffness in fractured patch interfaces.

In analogy with the methodology used for the structural coupling, the penalty approach is used also for enforcing continuity of the phase-field between the patch interfaces, as shown in Proserpio et al. [32]. Accordingly, the term

$$\int_{\mathcal{L}} \alpha_{PF}^{C^0} (s^A - s^B)(\delta s^A - \delta s^B)\, d\mathcal{L}, \tag{44}$$

which penalizes the difference of the phase-field at the two sides of $\mathcal{L}$, is added to the left-hand side of Eqs. (37) and (38) for guaranteeing C^0 continuity of s. If the higher-order phase-field formulation is employed, also C^1 continuity of s needs to be imposed between smooth patch interfaces. This can be achieved by summing to the left-hand side of Eq. (38), in addition to the aforementioned term for C^0 continuity, the following expression:

$$\int_{\mathcal{L}} \alpha_{PF}^{C^1} (\nabla s^A \cdot \mathbf{a}_n^A - \nabla s^B \cdot \mathbf{a}_n^B)(\nabla \delta s^A \cdot \mathbf{a}_n^A - \nabla \delta s^B \cdot \mathbf{a}_n^B)\, d\mathcal{L}, \tag{45}$$

which penalizes the relative change in the directional derivative of s along $\mathbf{a}_n$ between the two patches. The penalty imposition of C^1 continuity of s can only be applied to smooth patch interfaces. For this reason, the higher-order phase-field formulation cannot be used for structures including patch connections forming a kink, and the second-order model needs to be adopted. Because of the nonlinearity of the phase-field evolution equation, the first variation of Eq. (44), and of Eq. (45) if applicable, with respect to the discrete value of the phase-field at the control points s_r (so that $s_{,r} = \partial s / \partial s_r$), need to be added to the residual phase-field vector $\mathbf{R}_{PF}$:

$$\int_{\mathcal{L}} \alpha_{PF}^{C^0} (s^A - s^B)(s_{,r}^A - s_{,r}^B)\, d\mathcal{L}, \tag{46}$$

$$\int_{\mathcal{L}} \alpha_{PF}^{C^1} (\nabla s^A \cdot \mathbf{a}_n^A - \nabla s^B \cdot \mathbf{a}_n^B)(\nabla s_{,r}^A \cdot \mathbf{a}_n^A - \nabla s_{,r}^B \cdot \mathbf{a}_n^B)\, d\mathcal{L}. \tag{47}$$

Analogously, the second variation expressions:

$$\int_{\mathcal{L}} \alpha_{PF}^{C^0} (s_{,s}^A - s_{,s}^B)(s_{,r}^A - s_{,r}^B)\, d\mathcal{L}, \tag{48}$$

$$\int_{\mathcal{L}} \alpha_{PF}^{C^1} (\nabla s_{,s}^A \cdot \mathbf{a}_n^A - \nabla s_{,s}^B \cdot \mathbf{a}_n^B)(\nabla s_{,r}^A \cdot \mathbf{a}_n^A - \nabla s_{,r}^B \cdot \mathbf{a}_n^B)\, d\mathcal{L}, \tag{49}$$

need to be added to the phase-field tangent stiffness matrix $\mathbf{K}_{PF}$. As for the structural case, the penalty terms for imposing phase-field continuity between patches ($\alpha_{PF}^{C^0}$ and $\alpha_{PF}^{C^1}$) are chosen by scaling the global penalty parameter $\alpha_{glob} = 10^3$ with terms that maintain dimensional consistency with the related equation. At the same time, the penalty parameters need to be large enough in order to guarantee the imposition of the required continuity of s, without creating ill-conditioning in $\mathbf{K}_{PF}$. The history field $\mathcal{H}^e$ is the driving force of the phase-field equation and the term in which it is included becomes numerically predominant in the regions where fracture develops. Additionally, in cracked areas, the plastic strains usually increase up to a level comparable to α_{crit}, thus implying that $p = 1$. Considering that, for $p = 1$, the quadratic degradation function considered for brittle fracture is retrieved, we adopt the same penalty terms as for the brittle fracture case:

$$\alpha_{PF}^{C^0} = \alpha_{glob} \left[\frac{4\ell(1-\eta)\mathcal{H}_{max}^e}{t G_c} + 1 \right] h, \tag{50}$$

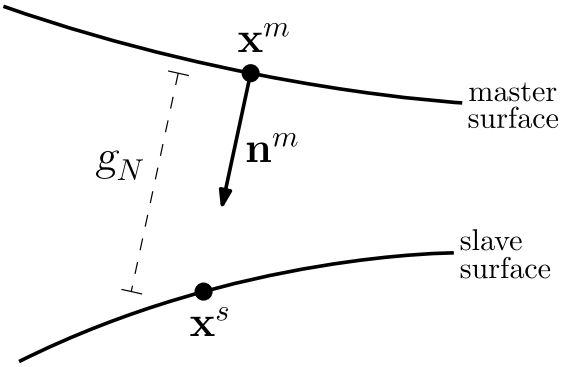

Fig. 2. Contact formulation, definition of the normal gap.

$$\alpha_{PF}^{C^1} = \alpha_{glob}\left[\frac{4\ell(1-\eta)\mathcal{H}^e_{max}}{tG_c} + 1\right]\ell^2 h. \tag{51}$$

The term $\mathcal{H}^e_{max}$ corresponds to the current maximum value of the history field in the structure.

As a final remark, we highlight that the penalty methodology presented in this section can be used also for weakly imposing clamping and symmetry boundary conditions.

2.5. Penalty-based frictionless contact formulation

In Section 4.2, we study a series of tests where different steel structures are penetrated by an indenter, simulating the consequences of ship grounding. For this reason, a frictionless penalty contact formulation suitable for large deformation problems is employed. We follow the approach outlined in Dimitri et al. [49], but instead of T-splines, LR NURBS (Locally Refined Non-Uniform Rational B-splines, see Section 2.6) are adopted for the discretization [50].

Two bodies, in this case two patches representing the shell midsurfaces, are assumed to be in contact. One of them is referred to as the *slave* surface and the other as the *master* surface. We assume that each point $\mathbf{x}^s$ on the slave surface can have only one partner contact point $\mathbf{x}^m$ on the master surface, whose position is computed by a closest point projection [51] of $\mathbf{x}^s$ over the master surface. The normal gap between the two surfaces is computed as:

$$g_N = (\mathbf{x}^s - \mathbf{x}^m)\cdot\mathbf{n}^m, \tag{52}$$

where $\mathbf{n}^m$ is defined as the normal unit vector at $\mathbf{x}^m$, with direction pointing towards the slave surface when no contact occurs, see Fig. 2. The direction of $\mathbf{n}^m$ remains constant during the analysis, even in case if the surfaces come into contact. According to the definition in Eq. (52), the normal gap is positive if the contact is open, while $g_N < 0$ in case of penetration. For thin shells and plates, instead of defining the contact between the midsurfaces, it is possible to describe the contact between the shell faces by taking into account the slave and master thicknesses, t^s and t^m respectively. In this case, $\mathbf{x}^s$ and $\mathbf{x}^m$ and the relative quantities continue to be defined at the midsurfaces, but contact starts occurring when $g_N < (t^s + t^m)/2$. Denoting with $\mathbf{T}$ the Piola traction vector, its normal component is the normal contact traction T_N:

$$\mathbf{T} = \mathbf{T}^m = -\mathbf{T}^s = T_N\mathbf{n}^m, \qquad T_N = \mathbf{T}\cdot\mathbf{n}^m. \tag{53}$$

The Kuhn–Tucker conditions for impenetrability are defined as follows:

$$g_N \geq 0, \qquad T_N \leq 0, \qquad g_N T_N = 0. \tag{54}$$

These contact constraints can be regularized by adopting the penalty formulation, and thus assume the form:

$$T_N = \alpha_N\langle g_N\rangle^-, \qquad \langle g_N\rangle^- = \begin{cases} g_N & \text{if} \quad g_N < 0 \\ 0 & \text{otherwise} \end{cases} \tag{55}$$

with α_N as the penalty parameter related to contact. Accordingly, the contribution of the frictionless contact formulation to the virtual work of the structure is defined as:

$$\delta W^{\mathrm{N}} = \int_{A^s} T_N \delta g_N \, dA = \alpha_N \int_{A^s} g_N \delta g_N \, dA, \tag{56}$$

with the integral evaluated on the slave surface in the reference configuration and δg_N representing the variation of the normal gap. For details regarding the variation and the linearization of the gap function and of the contact virtual work, and their discretization, the reader is referred to De Lorenzis et al. [52].

This contact formulation is denoted as "Gauss-point-to-surface", since the contribution to the virtual work δW^{N} is computed at each integration point of the slave surface. Contact between patches having non conforming meshes can be managed without any problem, as the master contact point $\mathbf{x}^m$ does not need to be a quadrature point. We adopt a pre-search algorithm that allows excluding, from the computation of the integral (56), slave elements which are sufficiently far from the master patch so that they are not affected by penetration, i.e. they do not contribute to δW^{N}. For each element on the slave surface, we identify the closest element on the master patch, whose center will be the starting point of the search algorithm for finding the contact point $\mathbf{x}^m$ of each integration point belonging to the considered slave element. This pre-computation makes the point search algorithm more efficient and prevents it from diverging, i.e. not finding the correct contact point. At this stage, we also compute the normal unit vector at $\mathbf{x}^m$ and we make sure that it is oriented in the correct way by inverting its direction if necessary, so that it can correctly represent $\mathbf{n}^m$. Once the direction of $\mathbf{n}^m$ is determined as the one pointing towards the slave surface (before contact occurs at $\mathbf{x}^m$), it is kept constant for the rest of the analysis.

In order to guarantee a scaling between the structural and the contact penalty stiffness when the penalty contact formulation is combined with the phase-field fracture approach, the effect of the phase-field degradation function is added into Eq. (56) by the term $g^{s,m}$, which takes the minimum value of the degradation function between the master and the slave contact points. The elements in the cracked zones have degraded material properties but still contribute to the contact penalty terms and, therefore, they provide resistance against penetration. In order to avoid this numerical problem and to remove fully broken elements from the contact computations, zero contact stiffness is guaranteed by imposing $g^{s,m} = 0$ if $s < 0.05$ at $\mathbf{x}^s$ or $\mathbf{x}^m$. So, the virtual work formulation in Eq. (19) is augmented by adding the following term:

$$\delta W^{\mathrm{N}} = \alpha_N \int_{A^s} g^{s,m} g_N \delta g_N \, dA. \tag{57}$$

2.6. Discretization of the geometry with LR NURBS

Thanks to the smoothness of the basis functions, IGA represents a favorable choice for the discretization of the geometry, because it allows for an efficient implementation of the rotation-free Kirchhoff–Love shell model and of the fourth-order phase-field formulation. In the context of the numerical simulation of contact, IGA allows for considering the exact geometry of the surfaces. Additionally, the higher continuity of the basis functions contributes to improving the performance of the contact algorithms, with respect to the traditional finite element implementations, thanks to the well-posedness of the closest-point projection problems [52].

In phase-field fracture analyses, the steep gradient of the smeared crack profile, whose width depends on the (often small) length scale parameter ℓ, requires a mesh having fine elements at least in the vicinity of the crack region. Due to their tensor product properties, the NURBS basis functions used in standard isogeometric analysis allow only a global refinement of the geometry. For this reason, we adopt a local refinement technology by employing LR NURBS [53], an extension of LR B-splines [54], for the discretization of the geometry. In this work, a ductile fracture formulation that employs a local plasticity theory is presented. Since mesh refinement is well known to be critical for local plasticity formulations [55], its influence is studied in Section 3.

2.7. Aspects related to the solution algorithm

From the stationarity condition of the energy functional (see Eq. (33)) with respect to the displacement field $\mathbf{u}$ and the phase-field s, the two governing equations of the coupled problem, i.e. the momentum and the phase-field evolution equations, are obtained. According to the staggered approach proposed by Bourdin et al. [3] and Miehe

et al. [5], the two equations are solved separately at each pseudo-time step of the analysis, keeping frozen the field which the equation is not solved for. In order to guarantee that the structure is in equilibrium at the end of each load step, we check the convergence of the solution after each staggered iteration and we repeat the process until the convergence is reached. It is important to point out that both the momentum and the phase-field equilibrium equations are nonlinear, so that they require an iterative solver. A classical approach, which will be called "loosely coupled" staggering scheme, would require, for each staggered iteration, first the iterative solution of the equilibrium equation for $\mathbf{u}$ and then the iterative solution of the phase-field equation for s. In order to improve the efficiency of the numerical simulation, we adopt the "strongly coupled" scheme, used in [32] for brittle fracture problems (where the phase-field equation is linear), according to which, in each staggered iteration, a single iteration of each of the two governing equation is performed, until convergence of the staggering process is reached (both for the momentum and the phase-field equation) with an adequately low tolerance for the residual. Box 1 outlines a comparison of the two approaches. The strong staggered coupling scheme is employed for all the numerical simulations of this paper.

Box 1: Loosely and strongly coupled staggering schemes. In case the convergence conditions are not satisfied, the iterations are repeated.

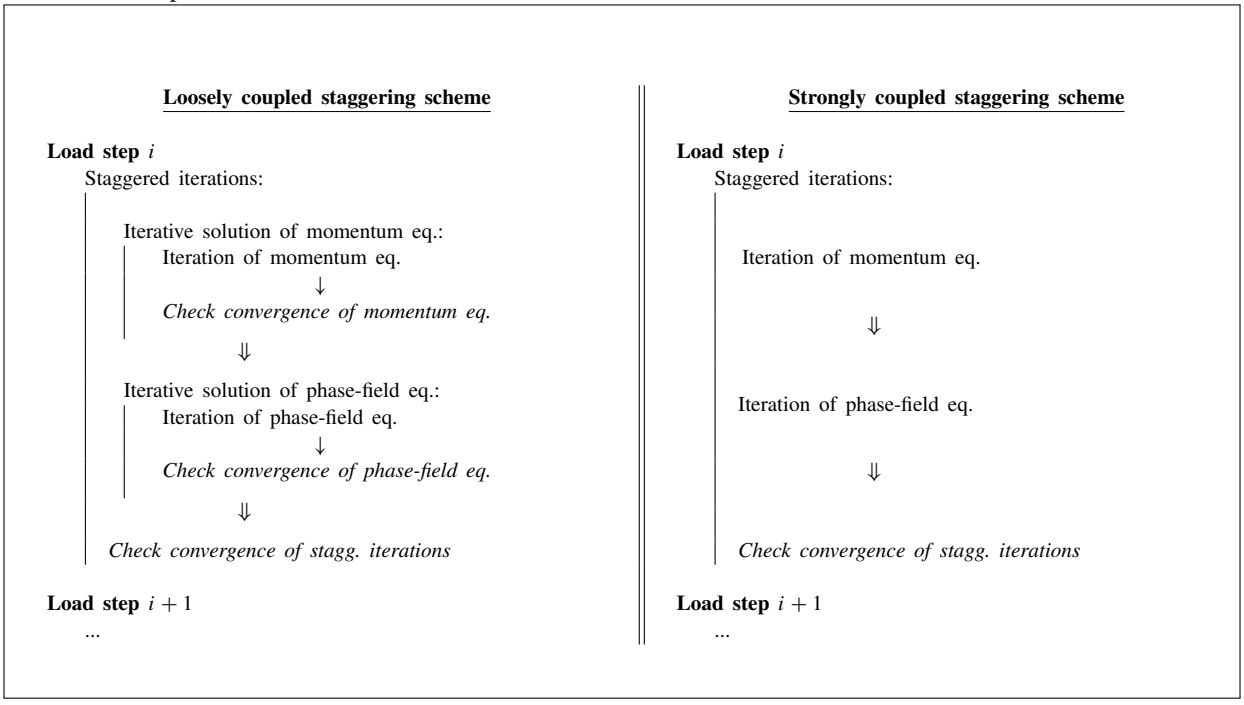

As observed by Gerasimov et al. [10] for phase-field brittle fracture analyses, when the staggering process is repeated until convergence in each step, the use of relatively large pseudo-time steps does not affect the results accuracy and even reduces the computational time, with respect to smaller steps. In order to improve the efficiency of the simulations, the use of quite large increments between the steps is possible in the initial part of the simulations or when the pure elastic regime dominates. On the other hand, large steps cannot be used when the plasticity starts evolving in the structure, otherwise no convergence of the momentum equation, and so of the staggered iterations, can be achieved. The same applies to the contact formulation, which cannot handle too large step increments that would lead to penetration at the beginning of the steps too large for allowing the convergence of the equilibrium equation. For these reasons, we adopt a simple adaptive step size procedure that will be briefly exposed. The initial step size is chosen as relatively large and represents the maximum possible step increment for the analyses. When a load step does not reach convergence (meaning that a maximum number of staggered iterations, set to 200 for the simulations presented in this work, is exceeded), the step is recomputed with an increment reduced by a factor of 2, until convergence is reached. In order to improve the efficiency of the simulations, we strive to have increments as large as possible. So, each time a step converges, we increase the step size by a factor 1.5 (we observed that

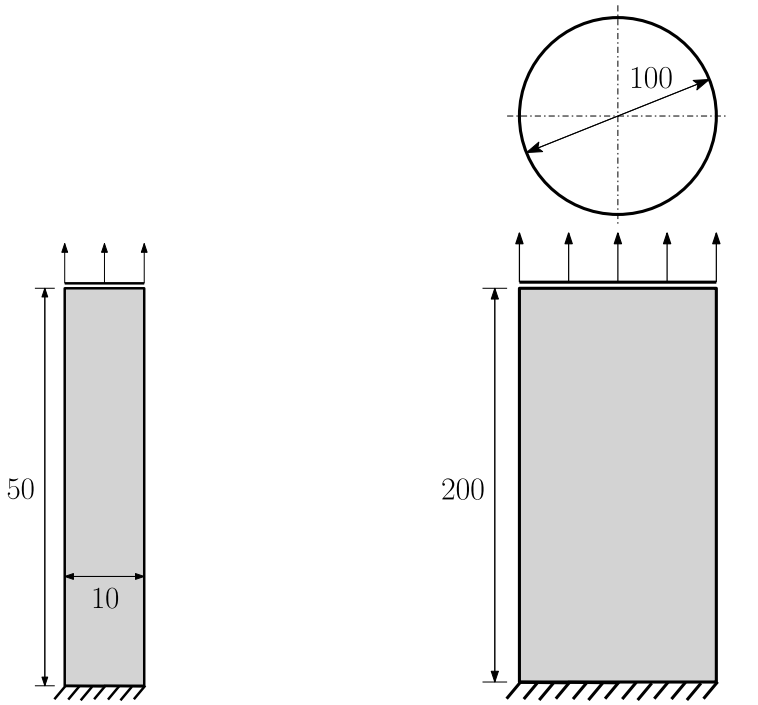

(a) Rectangular flat specimen (b) Hollow cylinder specimen

Fig. 3. Setup of the tensile problems (dimensions in mm).

an increase factor equal to the one for step reduction would often lead to non-convergence). The increment cannot, anyway, be larger than the maximum one set at the beginning of the analyses. This approach allows relatively large steps in the initial part of the analyses, while the increment size is reduced when complex deformations occur (for example the buckling of stiffeners in Section 4.2) or contact and phase-field ductile fracture effects dominate the simulation.

3. Adaptive local refinement for ductile fracture simulations

The J_2 plasticity formulation (see Section 2.1) employed in this work is a local plasticity model, meaning that the plastic constitutive equation of the material is evaluated at the integration points of the structure, without including any information about the size of the zone where plastic strains localize, because no length scale parameter is present in the model. As a consequence, the results of the simulations may be sensitive to the mesh size in the plastic region, which can localize differently and change dimension in case the mesh is refined [55].

3.1. Influence of the mesh size on the phase-field modeling of ductile fracture

In order to evaluate the effect of the mesh size on the considered local plasticity model combined with the phase-field fracture approach, we consider two numerical examples, a rectangular flat specimen and a hollow cylinder, under tensile loading caused by the imposed displacement of the top edge. Geometry and boundary conditions are shown in Fig. 3 (the thickness is $t = 1$ mm for both specimens). For the cylinder example, only one quarter of the model is simulated due to symmetry, employing symmetric boundary conditions imposed by penalty, according to the formulation in Section 2.4. The same J_2 plasticity model as in [45] with the following material parameters is considered in this work, i.e. $E = 189 \times 10^3$ N/mm^2 and $\nu = 0.29$ for elasticity. A nonlinear hardening law in the following form is assumed [17]:

$$R(\alpha) = \sigma_y + H_m\alpha + \left(\sigma_\infty - \sigma_y\right)\left(1 - e^{-\delta\alpha}\right), \tag{58}$$

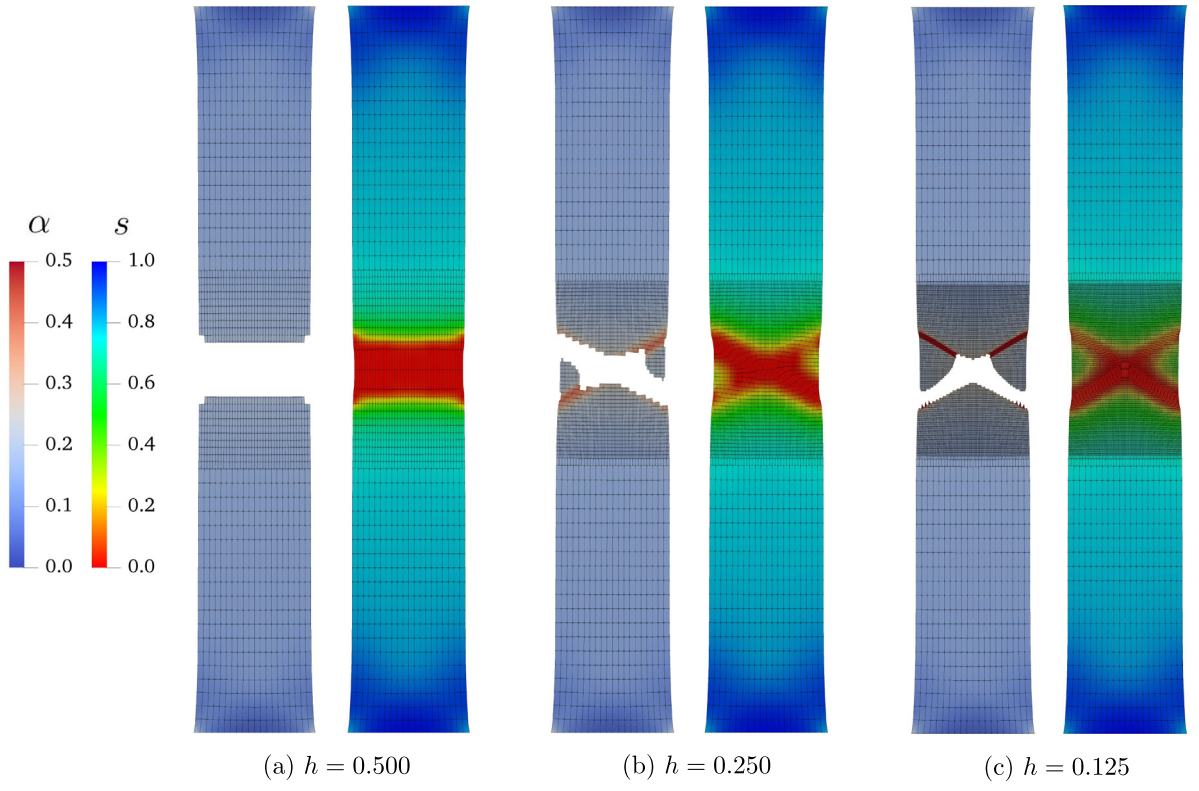

Fig. 4. Results of the phase-field ductile fracture simulations for the rectangular flat specimen with pre-refined mesh. The colormaps indicate the values of the hardening variable α and of the phase-field s. For visualization purposes, in the equivalent plastic strain plots, elements considered broken ($s < 0.05$) are removed. (For interpretation of the references to color in this figure legend, the reader is referred to the web version of this article.)

with yielding stress $\sigma_y = 343$ MPa, ultimate tensile strength $\sigma_\infty = 680$ MPa, hardening modulus $H_m = 300$ MPa, and saturation coefficient $\delta = 16.93$. The parameters required for the phase-field ductile fracture model are chosen as follows: fracture toughness $G_c = 1000$ N/mm, critical value of the hardening variable $\alpha_{crit} = 0.50$, $m = 1$, and $\ell = 0.50$ mm. The simulations are performed firstly only considering the elasto-plastic material model, then also including the phase-field ductile fracture formulation. Different mesh sizes are considered by employing local mesh refinement in the central region of the specimen, where necking, plastic strain concentration and fracture are expected to take place. For the rectangular flat specimen, we consider $h = \{0.500,\ 0.250,\ 0.125\}$ mm, where h indicates the minimum characteristic element size in the mesh. For the cylindrical geometry, $h = \{2.00,\ 1.00,\ 0.50\}$ mm is taken. In both cases, these minimum element sizes correspond to one, two or three levels of pre-refinement, respectively. For these and all the simulations in this paper, we use quadratic LR NURBS having 3 through-thickness integration points for each of the 3×3 Gauss points per element.

Figs. 4 and 5 show the results of the simulations involving phase-field fracture for the two specimens and the different meshes used. From the plots of the equivalent plastic strain α it is possible to notice that the plasticity accumulates in different ways as the mesh is refined. By using smaller elements, the concentration of the plasticity in shear bands can be captured. Since, according to the adopted phase-field formulation, the fracture starts evolving only in zones that undergo plastic strains, also the cracks will change shape and will start following the orientation of the shear bands as the mesh is refined. Figs. 6 and 7 show the load–displacement curves for the two specimens, both with only elasto-plasticity and with ductile fracture, for the considered element sizes. The results of the elasto-plastic simulations with and without phase-field fracture are the same until the points when the cracks start initiating and the curves of the phase-field simulations show a drop. Considering the simulations involving only J_2 plasticity, it is clear that the mesh refinement does not lead to convergence in the results. Even if all the curves are coincident in the

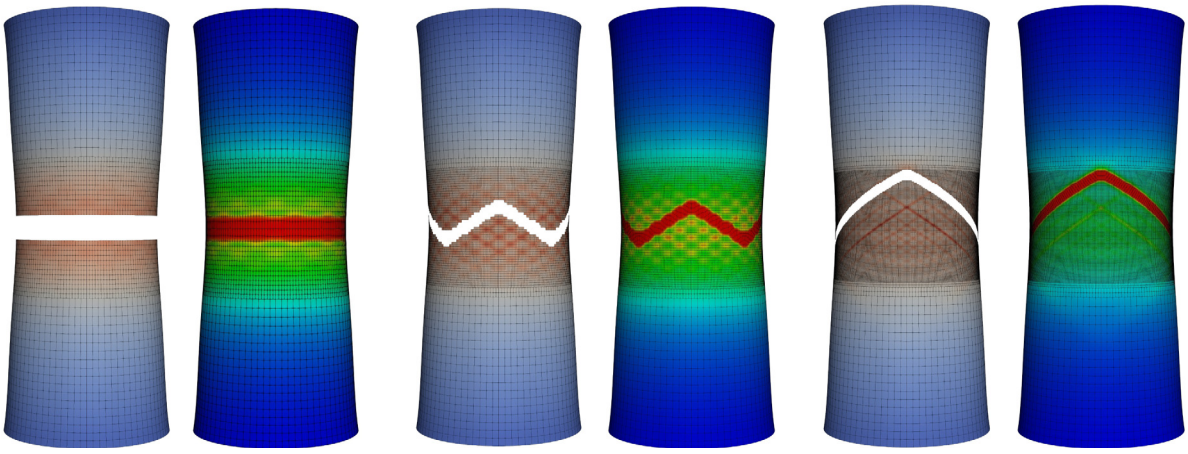

Fig. 5. Results of the phase-field ductile fracture simulations for the hollow cylinder specimen with pre-refined mesh. The colormaps indicate the values of the hardening variable α and of the phase-field s. For visualization purposes, in the equivalent plastic strain plots, elements considered broken ($s < 0.05$) are removed. (For interpretation of the references to color in this figure legend, the reader is referred to the web version of this article.)

first part of the analysis, after the occurrence of necking, finer meshes cause larger localization of the plastic strains in the necking region (following shear bands), leading to a softening behavior and to load–displacement curves showing less load-carrying capacity. The simulations involving phase-field fracture in addition to elasto-plasticity show instead load–displacement curves not too sensitive to mesh refinement, and convergence can be observed as the element size is reduced. It is important to recall that, according to the adopted phase-field ductile fracture model, plastic strains cease to concentrate when the fracture starts developing (only elastic deformation can take place in the fractured region). This means that, unlike for the pure elasto-plastic simulations, the plasticity cannot increasingly localize as the phase-field ductile fracture simulations proceed, thus alleviating the mesh dependency of the elasto-plastic model, even without adopting a non-local gradient formulation for plasticity. A possible interpretation of these results can also be related to the fact that the gradient term present in the phase-field model reduces the need of adopting a gradient plasticity formulation. In conclusion, we can assume that a local pre-refinement of the mesh can influence the direction and the shape of the fracture, but affects the simulated load–displacement curves of the specimens only up to a limited extent.

3.2. Adaptive local refinement strategy and validation

The use of an adaptive local mesh refinement scheme is crucial for performing phase-field fracture simulations on complex structures with a reasonable computational cost. In this section, we adopt the approach used in Proserpio et al. [32] for brittle fracture, and we test its validity in the framework of ductile fracture. The method consists in a predictor–corrector algorithm that allows refining the mesh only where needed, i.e. in the regions where the fracture is evolving, without knowing *a priori* where the cracks are going to nucleate and/or grow. According to the algorithm, which is summarized in Fig. 8, at the end of each step we evaluate whether the mesh needs to be refined. If this is the case, the mesh refinement is performed, the solution of the precedent step is transferred to the refined mesh and the considered step is recomputed with the new mesh. Unlike for the brittle fracture case, in ductile fracture simulations cracks often grow during several steps, meaning that the evolution of the fracture during a single step is relatively limited (even when the convergence of the staggered iterations is achieved). Nevertheless, it may happen that, at the end of a recomputed step, the crack has grown outside of the region just refined. In this case, the load step needs to be recomputed again, and the process is repeated until there is no need for further refinement.

The need for refinement is evaluated according to the fact that ductile fracture is preceded by a concentration of the plastic strain, which is measured by the hardening variable α. For this reason, we choose the equivalent

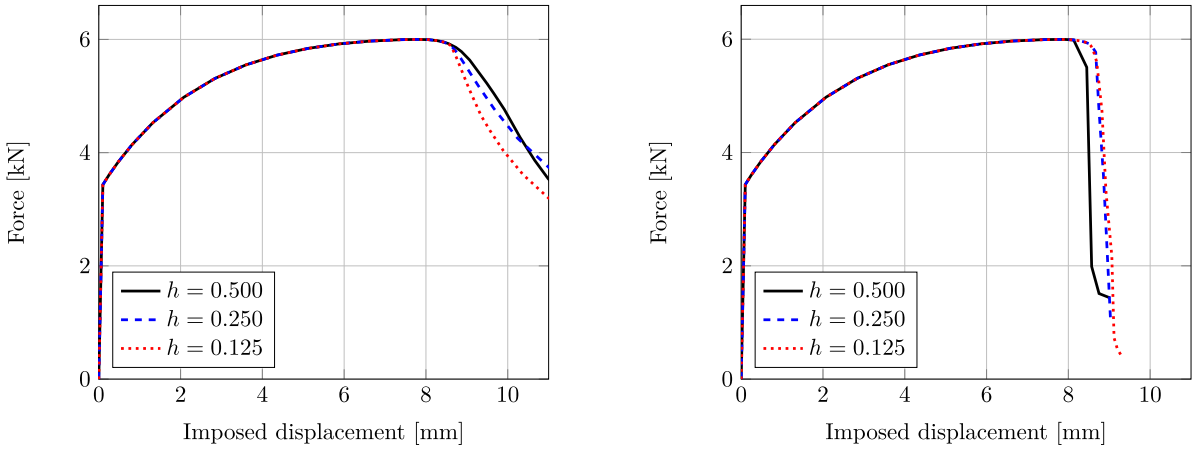

(a) Elasto-plasticity (b) Phase-field ductile fracture

Fig. 6. Load–displacement curves of the elasto-plastic simulations with and without phase-field fracture formulation for the rectangular flat specimen with pre-refined mesh.

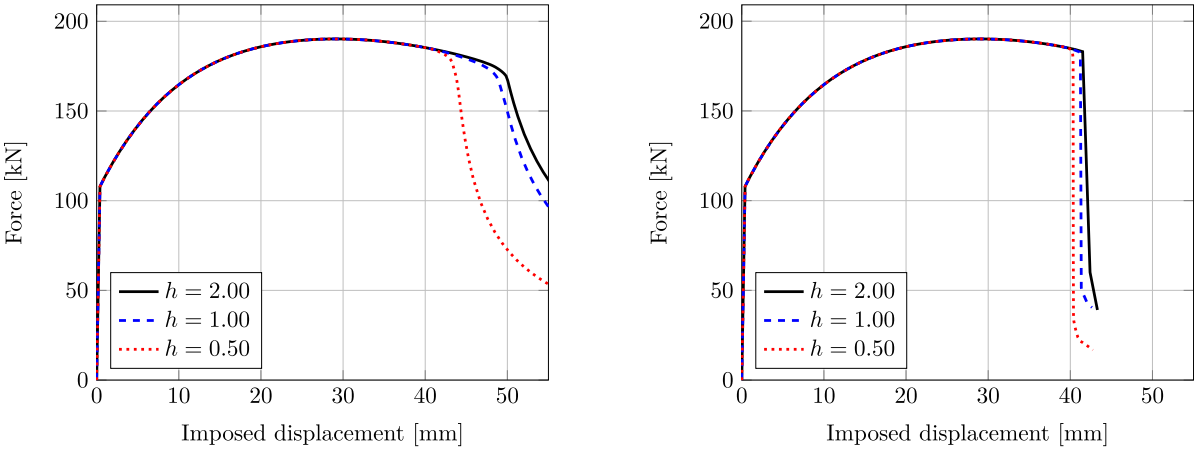

(a) Elasto-plasticity (b) Phase-field ductile fracture

Fig. 7. Load–displacement curves of the elasto-plastic simulations with and without phase-field fracture formulation for the hollow cylinder specimen with pre-refined mesh.

plastic strain α as the indicator for the refinement and, at the end of each load step (including recomputed ones), we mark for refinement all the elements that are larger than the prescribed minimum element size and in which the value of the hardening parameter is higher than a threshold value, i.e. $\alpha > \alpha_t$ at least in one integration point. Since we want to be able to capture the localization of plasticity, that can potentially lead to cracks following shear bands (see Section 3.1), we adopt a conservative approach so that the mesh is refined before the onset of fracture. Therefore, the value $\alpha_t = 0.25\,\alpha_{crit}$ is chosen and used in all the simulations of this paper including adaptive mesh refinement. The refinement is performed according to the "structured mesh" strategy [54], which consists in splitting all the knot spans of the support of a certain basis function. This approach provides a regular mesh, with a good transition between zones having different element sizes, and keeps the aspect ratio of the elements in parametric space constant.

For each refinement round, it is necessary to transfer all the state variables from the coarse to the refined mesh. The field quantities defined at the control points (displacement $\mathbf{u}$ and phase-field s, which are also the unknowns

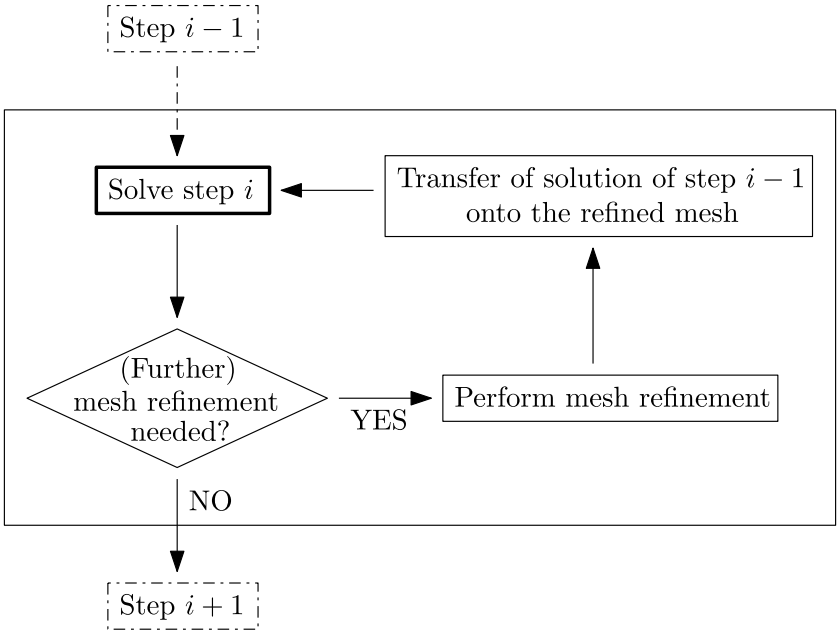

Fig. 8. Adaptive local refinement algorithm.

of the coupled problem) are projected according to the same algorithms used for determining the coordinates of the control points corresponding to split basis functions [54]. The history field $\mathcal{H}^e$, the hardening variable α, the thickness stretch λ_3, and the plastic right Cauchy–Green deformation tensors $\mathbf{C}^p = \mathbf{F}^{pT}\mathbf{F}^p$ are instead quantities defined at each thickness integration point [45]. The transfer of these quantities, from the integration points of the coarse element to the ones of the refined elements having the same position across the thickness, is performed for each scalar variable according to a local Bézier-element-based interpolation [32,56]. For the right Cauchy–Green deformation tensor, the transfer is operated separately for each component.

We test the effectiveness of the adaptive local refinement procedure on the two numerical examples previously run for verifying the effect of the mesh pre-refinement (see Section 3.1). In both cases, two levels of adaptive mesh refinement are employed, for a minimum mesh size $h = 0.250$ mm for the rectangular flat specimen and $h = 1.00$ mm for the hollow cylinder example. Fig. 9 shows the initial mesh and the final results of the simulations for the two geometries, which can be compared with the ones from the simulations with pre-refinement of the mesh (Figs. 4(b) and 5(b)). The mesh refinement is performed early enough in order to capture the localization of the plastic strains and therefore the cracking develops along the shear bands. Due to the conservative choice of the indicator for the refinement and due to the uniform geometry of the specimens subjected to tensile test, a widespread region of the domain is refined in both cases. In the rectangular flat specimen, some local refinement occurs also at the corners due to plasticity localization, but this does not lead to fracture in those locations. Fig. 10 shows a good agreement of the load–displacement curves between the simulations employing adaptive local refinement and the corresponding ones performed with a pre-refined mesh. For the examples presented in this section, the reduction of the computational cost due to the adoption of the adaptive refinement is limited by the fact that a large portion of the mesh needs to be refined. The examples in Section 4 will show the importance of adaptive refinement for structures where the cracked area covers only a small part of the total domain.

4. Numerical examples with experimental validation

We now validate our method by simulating two different experimental tests and by comparing the results of the analyses with the experimental ones available in the literature. The first example (Section 4.1) features a pre-cracked steel plate subjected to out-of-plane loading, while the second one (Section 4.2) includes a series of indentation tests conducted on stiffened steel panels.

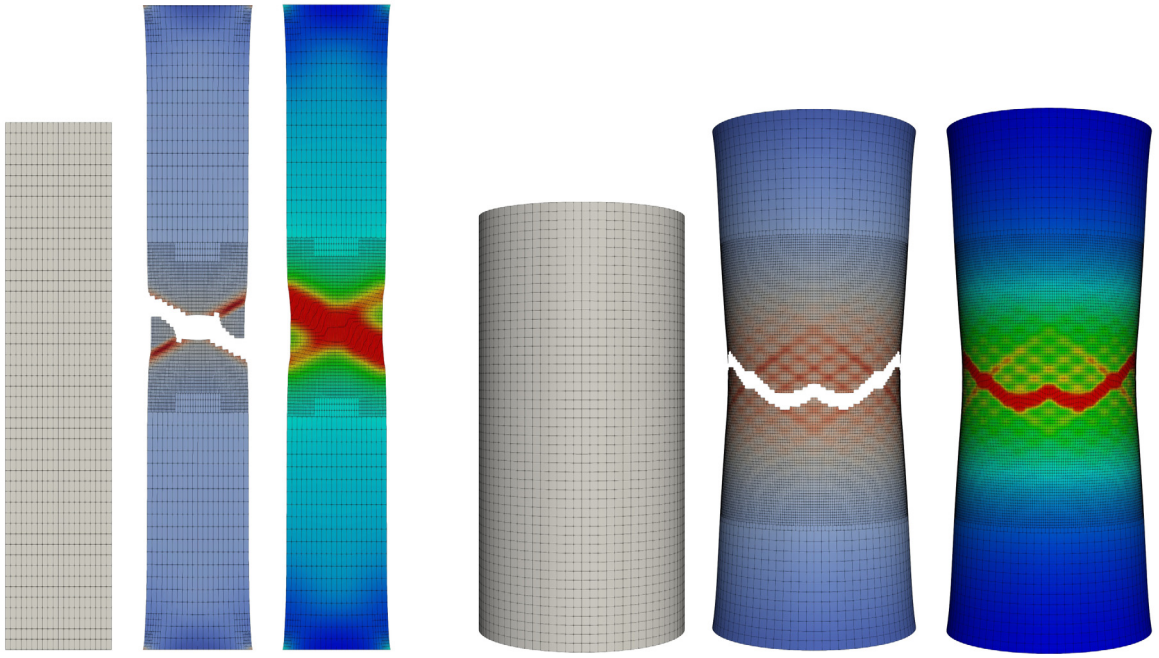

(a) Rectangular flat specimen, $h = 0.250$ mm

(b) Hollow cylinder specimen, $h = 1.00$ mm

Fig. 9. Results of the phase-field ductile fracture simulations employing adaptive mesh refinement for the tensile specimens in the terms of hardening variable and phase-field. The colormaps indicate the values of the hardening variable α and of the phase-field s. For visualization purposes, in the equivalent plastic strain plots, elements considered broken ($s < 0.05$) are removed. (For interpretation of the references to color in this figure legend, the reader is referred to the web version of this article.)

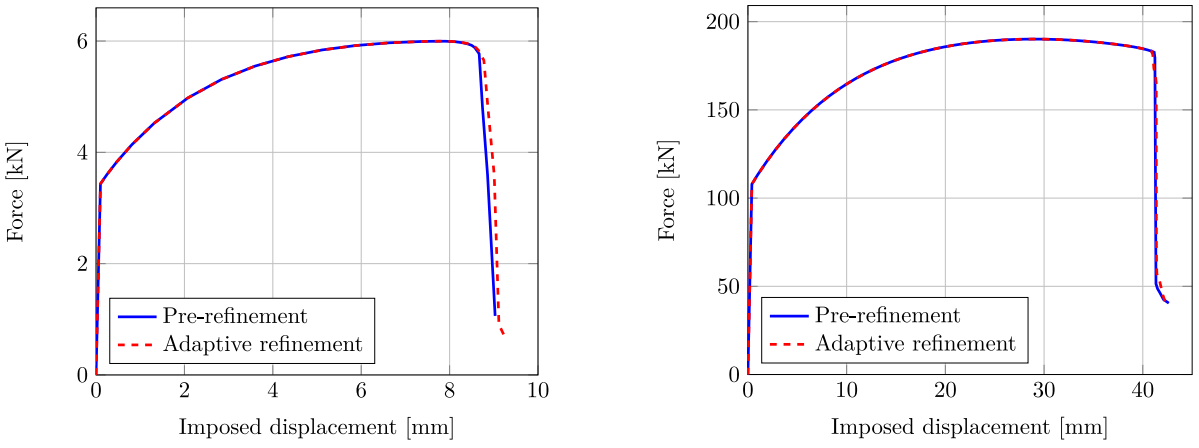

(a) Rectangular flat specimen, $h = 0.250$ mm

(b) Hollow cylinder specimen, $h = 1.00$ mm

Fig. 10. Comparison of the load–displacement curves from the phase-field ductile fracture simulations with and without adaptive mesh refinement for the tensile specimens.

4.1. Tearing of a plate by out-of-plane loading

We consider a square plate made of steel with a pre-crack, teared by the action of a couple of transverse point loads. The problem has been experimentally tested by Muscat-Fenech and Atkins in [57]. The geometry and the

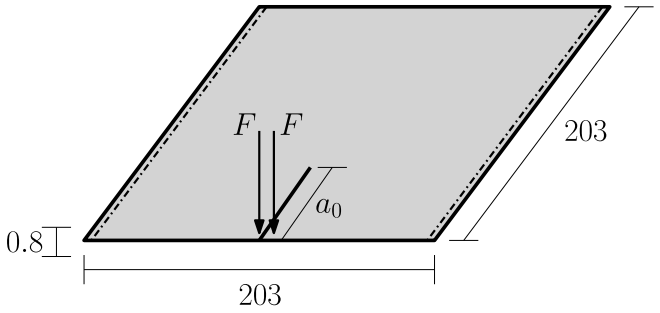

Fig. 11. Setup of the plate tearing problem (dimensions in mm). Black dash-dotted lines indicate clamped edges.

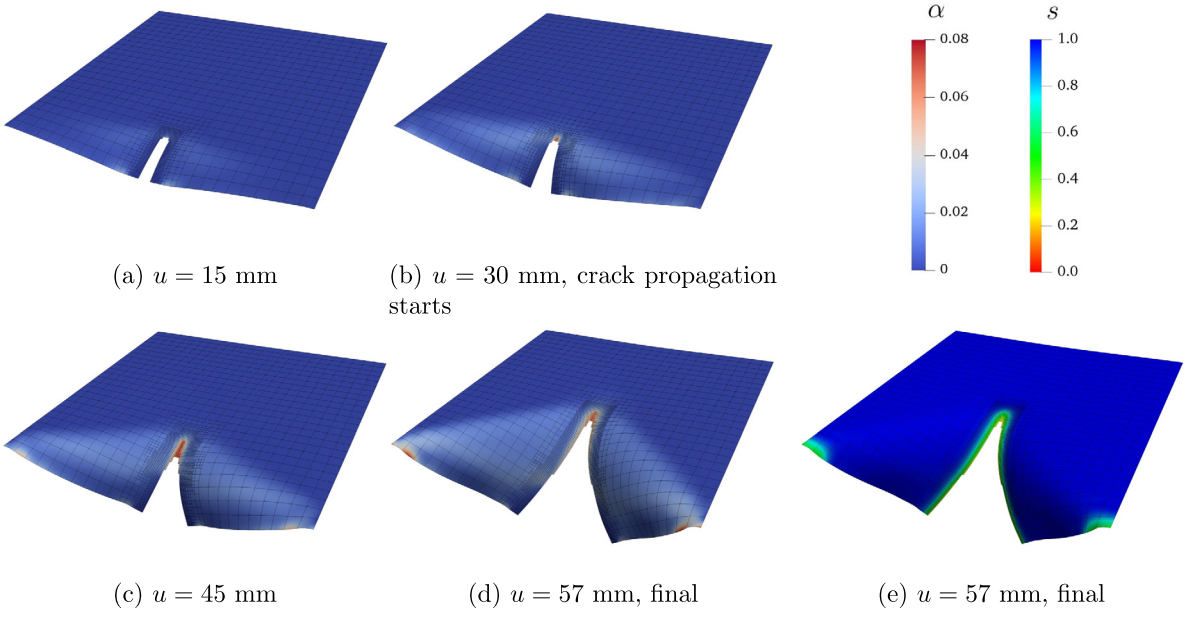

Fig. 12. Results of the simulation of the tearing of the plate at different moments of the analysis (indicated by the value u, the transverse displacement of the points where the loads are applied). For visualization purposes, the fully broken elements are removed from the plate. The colormaps indicate the value of the hardening variable α and of the phase-field s. (For interpretation of the references to color in this figure legend, the reader is referred to the web version of this article.)

boundary conditions (clamping is imposed by penalty, see Section 2.4) are outlined in Fig. 11 and a pre-crack length $a_0 = 30$ mm is considered. The elasto-plastic material parameters are assumed as the one used in [58], where the example has been numerically investigated using an extended finite element methodology: Young's modulus $E = 210 \times 10^3$ N/mm^2, Poisson's ratio $\nu = 0.30$, hardening law

$$R(\alpha) = 574\,(0.010372 + \alpha)^{0.26}, \tag{59}$$

fracture toughness $G_c = 255$ N/mm, critical value of the hardening variable $\alpha_{crit} = 0.045$. The fourth-order phase-field model is employed with length scale parameter $\ell = 2.0$ mm and adaptive local mesh refinement, for the crack developing in the central region of the specimen, is adopted according to the strategy explained in Section 3.2, with three levels of refinement leading to a minimum element size $h = 1.0$ mm, so that $h = \ell/2$.

Fig. 12 shows the specimen at different moment of the analysis. The crack growth starts at the moment when the displacement u of the points where the loads are applied is equal to 30 mm (see Fig. 12(b)), a good correspondence with the experimental results reporting 31 mm. The analysis is terminated at $u = 57$ mm (see Figs. 12(c) and 12(f)), when the applied load reaches the maximum value reported in the experimental reference $2F = 1800$ N.

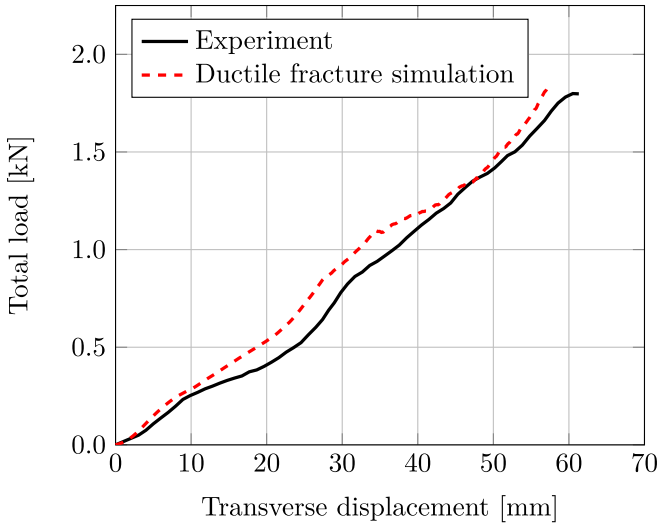

Fig. 13. Comparison of the load–displacement curves for the plate tearing problem.

The experimental and numerical load–displacement curves in Fig. 13 show good matching of the results. Despite including large deformations, plastic strains development and large crack growth, the curves appear almost straight. This shape is different with respect to the curves presented in the previous section, which were more similar to the response curves of the employed material model due to the tensile setup of the tests.

4.2. Application to complex structures: indentation tests on stiffened panels

We consider a series of experimental indentation tests on steel panels performed by Alsos et al. [59]. The experimental campaign was conducted in order to evaluate the resistance of stiffened plates from ship hulls in case of events like ship grounding. Section 4.2.1 presents the setup of the problem, while in Section 4.2.2 the results of the simulations are compared with the experimental ones and then discussed.

4.2.1. Problem definition and setup of the simulations

The experimental campaign from which we extract the experimental benchmarks consists in a series of indentation tests performed on rectangular steel panels. The experimental setup is shown in Fig. 14. Different plate configurations are considered: unstiffened panel (US), panel with one flat bar stiffener (1-FB), and panel with two flat bar stiffeners (2-FB). For both the 1-FB and 2-FB case, the stiffeners are welded to the plate. In the experimental setup, the panel and the ends of the stiffeners are welded to a strong frame consisting of massive steel boxes. We choose to include in the simulations only the plates and the stiffeners, and we model their connections to the frames employing clamped boundary conditions (imposed by penalty, see Section 2.4), as it can be assumed that the surrounding girder webs are stiff enough to represent a rigid support [59]. The dimensions and geometry of the panels and of the indenter are depicted in Fig. 15. The thickness of the plate is 5 mm, while the thickness of the stiffeners is 6 mm.

The material of the plate and of the stiffeners consists in rolled mild steel, namely S235JR EN10025. Stress–strain curves, resulting from tensile tests performed on samples extracted from the same batch from which the tested structure was manufactured, are published [59]. The tensile tests have been performed in directions both parallel and perpendicular to the rolling direction. From the average of the two responses, the experimental curve shown in Fig. 16 is obtained. Apart from the elastic properties, which are taken as the well known ones for mild steel ($E = 210 \times 10^3$ N/mm^2, $\nu = 0.30$), numerical simulations of the tensile tests are necessary in order to determine, by comparison with the available experimental curve, the plasticity and fracture parameters of the material. The elasto-plasticity model without phase-field fracture employing a nonlinear hardening law as in Eq. (58) is adopted for the quantification of the plasticity properties, which result in yielding stress $\sigma_y = 285$ MPa, ultimate tensile

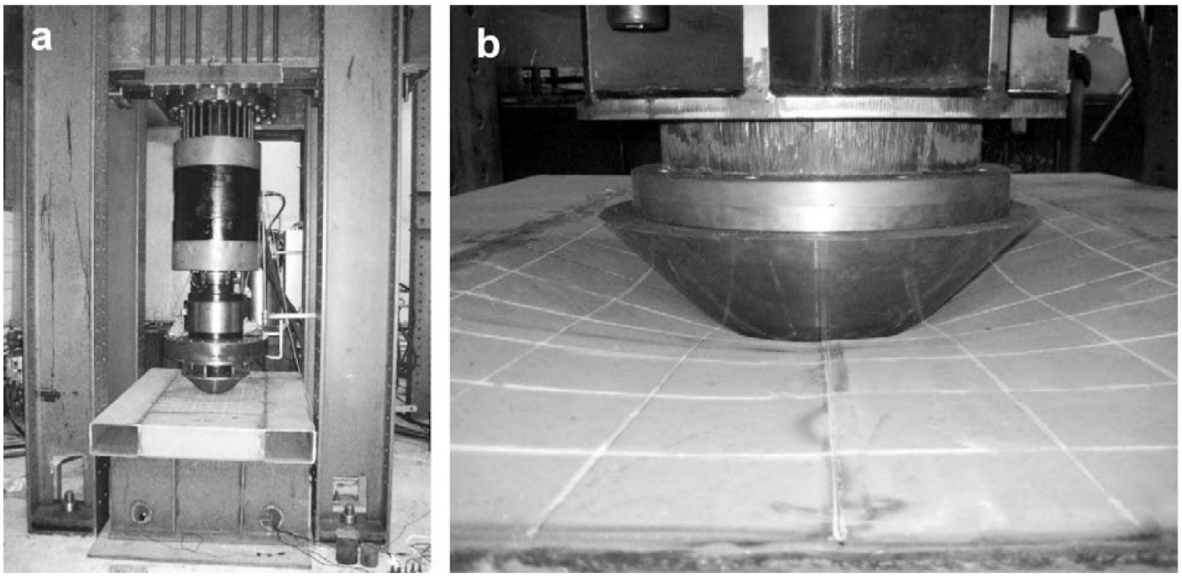

Fig. 14. Experimental setup for the indentation test. (a) shows a tested panel with its box beam frame in the experimental rigging, that includes a hydraulic jack mounted on a crosshead and the indenter. (b) shows the interaction between the indenter and the plate during the test [59][§].

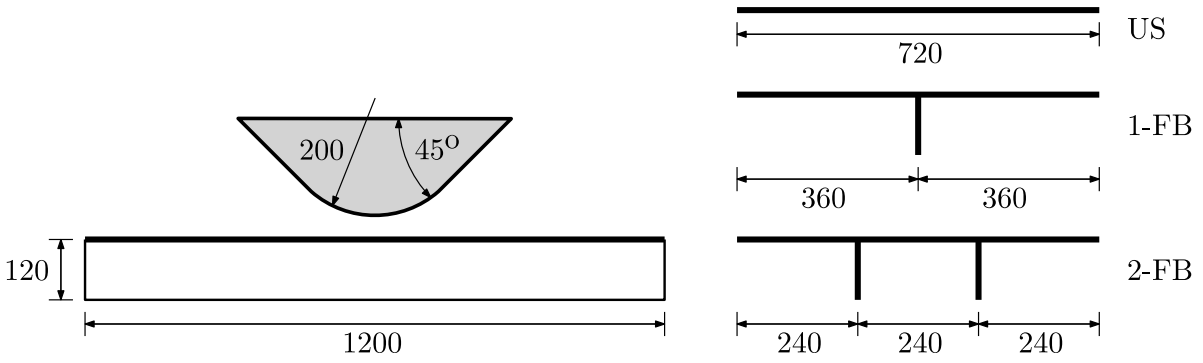

Fig. 15. Longitudinal view of a stiffened plate with the indenter and transversal view of the three panel configurations (dimensions in mm).

strength $\sigma_\infty = 395$ MPa, hardening modulus $H_m = 550$ MPa, and saturation coefficient $\delta = 25.00$. Once these values are set, ductile fracture simulations are performed for determining the fracture toughness as $G_c = 35$ kN/mm, the critical value of the hardening variable as $\alpha_{crit} = 2.0$, and $m = 1$. Fig. 16 shows the stress–strain curves from the simulations employing these parameters, in comparison with the one obtained from the experiments on the specimens. The material parameters determined in this section will be used as input for the numerical modeling and for predictions of the results of the indentation tests.

The simulations of the indentation tests are performed in displacement control, imposing the displacement of the indenter in the direction perpendicular to the plate. In the experimental campaign, the displacement rate of the cylinder was set to 10 mm/min in order to minimize the strain rate effects, which can be considered negligible as they are supposed to account for an increase in loads of $2-4$ % with respect to the static scenario [59]. For this reason, the analyses are performed in the quasi-static regime. Despite the better efficiency of the fourth-order phase-field model, especially in connection with adaptive local refinement [32], the higher-order formulation can be employed only for the US analysis, where no patch connections with kinks are present. The second-order phase-field model is used instead for the 1-FB and 2-FB cases, because of the non-smooth patch connections between the panel and the stiffener, which prevent the imposition of the C^1 continuity of s (see Section 2.4). The length scale

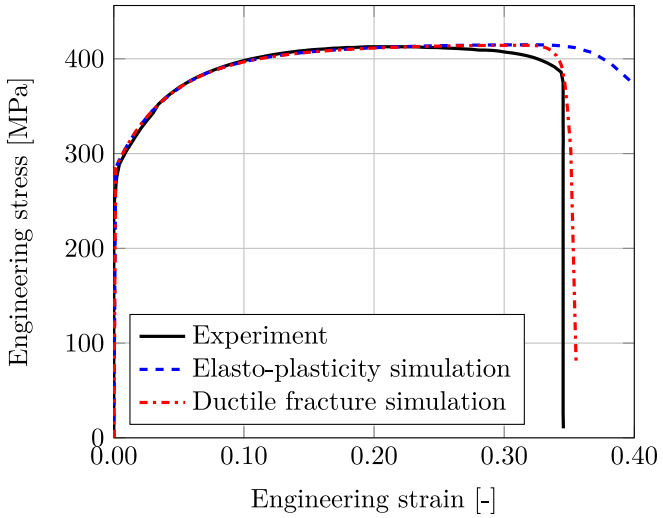

Fig. 16. Stress–strain curves for the tensile test and simulations used for evaluating the material properties, according to the adopted computational model, of the mild steel rolled plates employed in the indentation test.

parameter for the phase-field model is taken as $\ell = 6$ mm. Adaptive local mesh refinement according to the strategy explained in Section 3.2 is adopted, with three levels of refinement leading to a minimum element size $h = 3$ mm, so that $h = \ell/2$. Due to the symmetry of the setup and considering that the experimental results showed a symmetric behavior, only half of the geometry is simulated, with the symmetry plane passing at the transverse center line of the plate. Since the model involves another symmetry plane (corresponding to the panel center line, in the longitudinal direction), the perfectly symmetric setup makes the nucleation of localized cracks difficult, in the simulations. For this reason, we introduce an imperfection in the model in the form of a small pre-crack located along the transversal symmetry plane. In addition, the indenter tip is supposed to hit the center of the panels, but assuming that some offset between the indenter position and the target center is present in the testing, the indenter position is shifted by 5 mm from the panel center, along the transversal symmetry plane, in the simulations setup. Patch coupling, symmetry and clamping boundary conditions are applied by employing the penalty formulation (Section 2.4). In the experimental setup, the indenter is milled out from a solid piece of steel, therefore, in the simulations, only its lower surface is modeled and it is considered as a rigid shell. Contact conditions are simulated according to the frictionless penalty formulation exposed in Section 2.5. In addition to the plate-indenter and the plate-stiffeners interactions, due to the possibility of penetration caused by the damage of the panel elements involved in the contact, the contact between the indenter and the stiffeners has to be taken into account as well. Shell thickness is considered in the contact computations for the panel and the stiffeners. The contact penalty parameter is set as $\alpha_N = 10^3$.

4.2.2. Simulation results and discussion

Fig. 18 shows the result of the simulation for the unstiffened plate in the undeformed and deformed configuration. The fracture starts at approximately 100 mm from the center line in the longitudinal direction (referring to the undeformed configuration) and evolves with a shape similar to the one observed during the benchmark experimental tests (Fig. 17(a)). It can be noted that some mesh refinement occurs around the plate center due to the increase of the plastic strain in that region. Nevertheless, this does not lead to fracture, showing that the refinement of the mesh does not necessarily imply the onset of cracks. In the 1-FB case (Fig. 19), the stiffener, which is placed in the middle of the panel, is initially subjected to bending and shear action, until buckling and consequent folding occur at approximately 130 mm of displacement of the indenter. Therefore, the stiffener does not break, while the fracture happens in the plate, close to the connection with the stiffener itself, as observed in the tests (Fig. 17(b)). For the 2-FB geometry, the fracture occurs in the area between the two stiffeners and evolves in a way similar to the unstiffened case. No stiffeners failure is again observed, nor in the experiments neither in the simulations, as shown in Figs. 20 and 17(c). The buckling of the stiffeners can be observed at approximately 65 mm of displacement of the indenter. The comparison of the load–displacement curves resulting from the indentation tests and the simulations

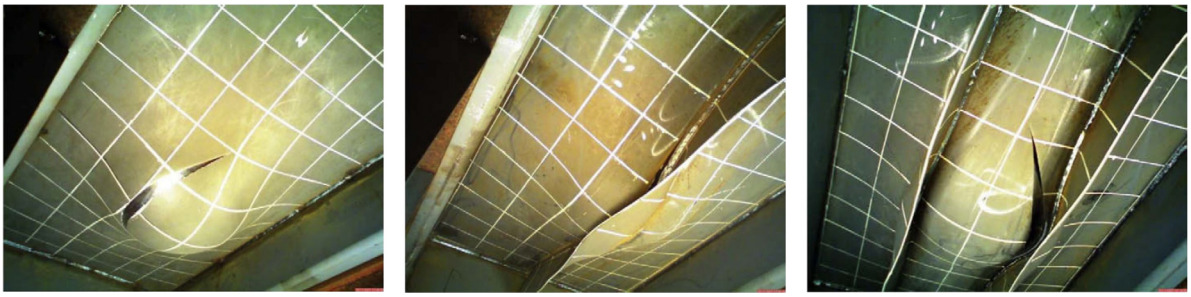

(a) US (b) 1-FB (c) 2-FB

Fig. 17. Results of the indentation tests on the three panel configurations. [59][§].

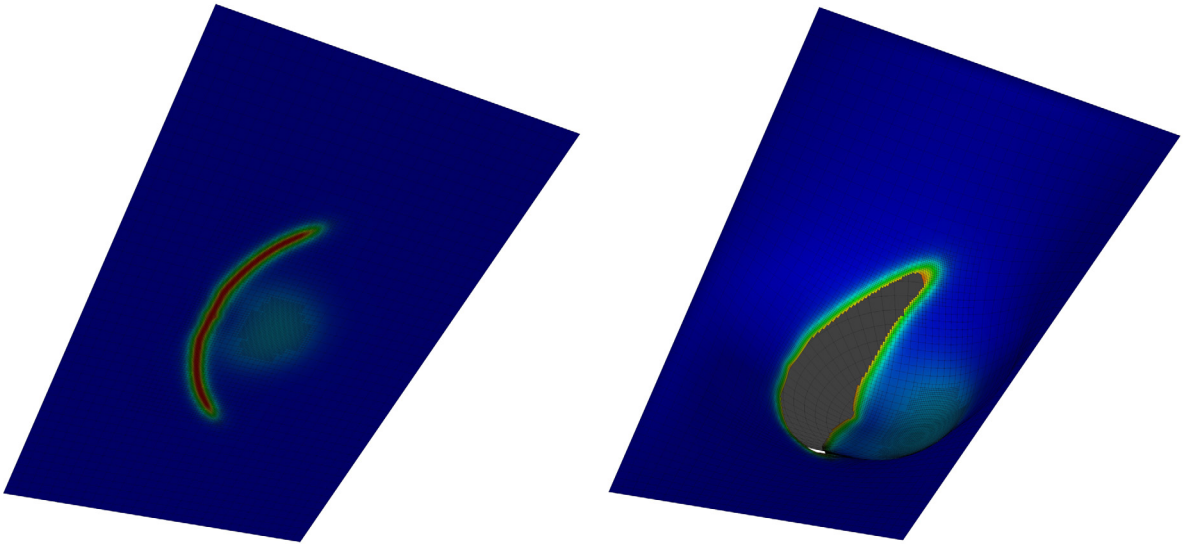

(a) Undeformed configuration

(b) Deformed configuration. For visualization purposes, the fully broken elements are removed from the plate. The indenter is represented with a different colormap.

Fig. 18. Result of the simulation of the indentation test on the US panel. (For interpretation of the references to color in this figure legend, the reader is referred to the web version of this article.)

performed for this paper is shown in Figs. 21 and 22. In the experimental setup, the force and the displacement were measured on the crosshead of the hydraulic jack that acts on the movement of the indenter. Since the simulations are conducted in (increasing) displacement control, we removed from the experimental curves the part referring to the retraction of the indenter. There is good agreement between the curves in the first part of the analyses, which include the initial elastic deformation, the nonlinearity due to the onset and development of plasticity, the contact between the indenter and the plate, the buckling of the stiffeners (if present), and the crack development (detailed considerations regarding the fracture mechanism for this example can be found in [59,60]). Significant plastic strains appear already after 20 mm indentation, while the first crack growth can be observed after 135 mm, 118 mm and 104 mm of indentation for the US, 1-FB and 2-FB panels, respectively. The simulations predict the failure moment with reasonable precision in the US and 1-FB cases, and with good estimates of the peak load with respect to the experimental curves. The two-stiffeners panel simulation, instead, overestimates the maximum load carried by the structure and predicts a too late fracture.

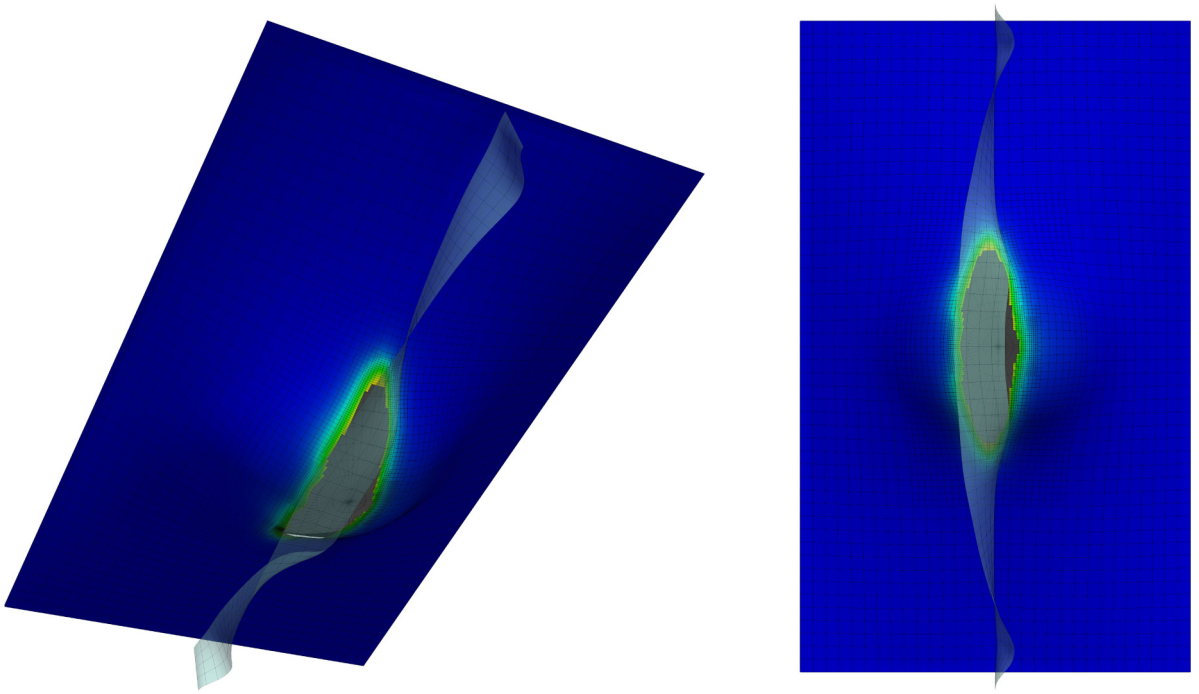

Fig. 19. Result of the simulation of the indentation test on the 1-FB panel from two different viewpoints. For visualization purposes, the fully broken elements are removed from the plate. The indenter and the stiffener are represented with different colormaps. (For interpretation of the references to color in this figure legend, the reader is referred to the web version of this article.)

Among the factors that influence the not perfect matching of the curves, we recall that a frictionless contact formulation is employed, while the presence of static friction should be assumed between the steel surfaces of the indenter and of the plate. Moreover, the larger difference between the experimental and the simulation curves of the 1-FB and 2-FB cases compared with the unstiffened case can be related to the fact that the simulations do not include the modeling of the stiffeners weld bead. Fracture was never experimentally observed in the weld material, but the modeling of the weld bead would make the simulated structure stiffer. The post-failure resistance shown by the numerical curves can be related to a redistribution of the internal actions in the main plate from the transverse to the longitudinal direction, as a consequence of the development of the crack. This factor, together with the ductility of the material and the quasi-static regime of the analyses, can explain the shape of the load–displacement curves. This behavior is more evident than in the results from the analyses performed on the tensile specimens, see Fig. 16, where it is possible to describe the drop of the load–displacement curve. The adoption of an enriched model could be useful for replicating this behavior also for the considered structure. However, considering the complexity of the model, the numerical simulations provide satisfactory predictions of the behavior of the stiffened plates both in terms of crack path and load–displacement curves. The result is relevant, especially taking into account the fact that the material parameters of the model have been determined only from the results of the tensile tests performed on the specimens of the material considered in the experiments. Considerations similar to the ones after the experimental campaign can be drawn from the performed simulations. First of all, the initiation of fracture does not imply a total loss of the resistance of the structure. Moreover, the presence of one or more stiffeners obviously increases the initial stiffness of the panels and reduces their flexibility, at the price of earlier fracture and less maximum carried load.

5. Conclusion

We have presented an approach for the simulation of ductile fracture in shell structures. An isogeometric rotation-free Kirchhoff–Love shell formulation was combined with an elasto-plasticity material model and with a phase-field ductile fracture formulation at finite strains, here extended to the higher-order version. According to this approach,

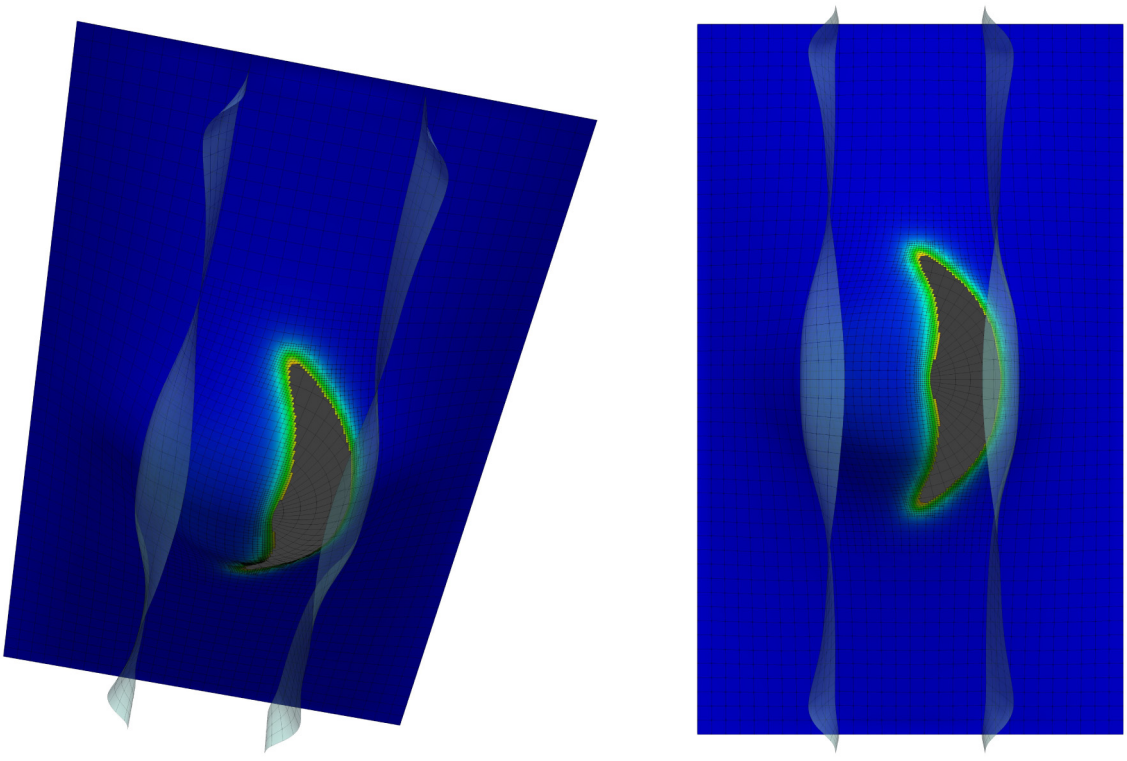

Fig. 20. Result of the simulation of the indentation test on the 2-FB panel from two different viewpoints. For visualization purposes, the fully broken elements are removed from the plate. The indenter and the stiffeners are represented with different colormaps. (For interpretation of the references to color in this figure legend, the reader is referred to the web version of this article.)

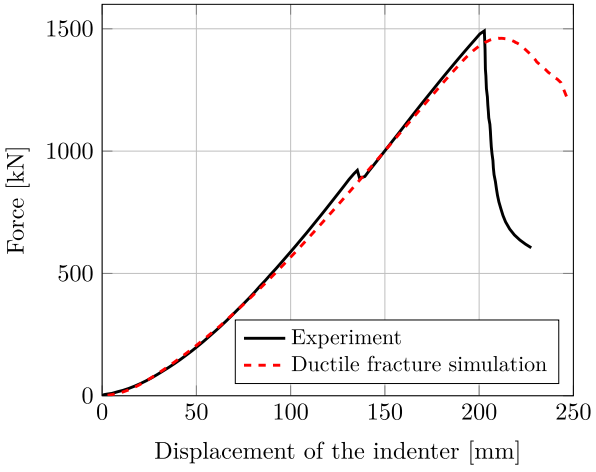

Fig. 21. Comparison of the load–displacement curves for the indentation test on the US panel.

it is possible to describe, with a single value of the phase-field defined at the midsurface, a nonlinear distribution of the stress tensor and a degradation function varying through the shell thickness.

In order to simulate the failure of geometrically complex multipatch structures, we adopted a penalty formulation for coupling the structural and the phase-field fracture behaviors across the patch interfaces. A penalty formulation has been also employed for the simulation of frictionless contact conditions. Being used in phase-field fracture simulations, both the penalty formulations had their terms scaled by the phase-field degradation function, in order to

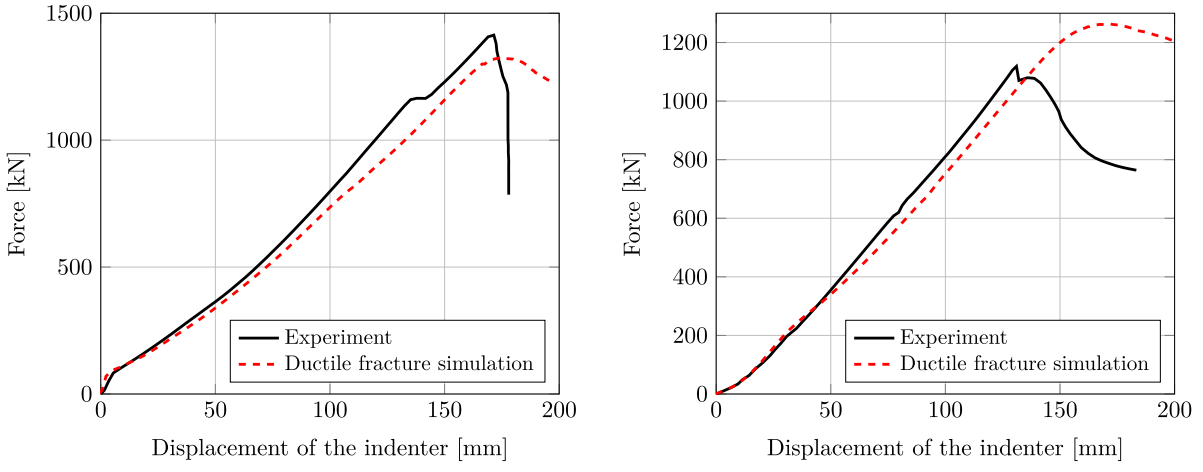

(a) 1-FB (b) 2-FB

Fig. 22. Comparison of the load–displacement curves for the indentation tests on the stiffened panels.

maintain the numerical proportion between structural and penalty stiffness during the analyses and in order to relax the penalty constraints in the fractured zones. Additionally, we found that fractured elements have to be removed from the contact algorithms for enabling penetration. The adequate choice of the penalty terms was suggested by the stability and convergence of the numerical analyses performed.

Despite the strong mesh dependency of the local plasticity model, the mesh sensitivity of the ductile failure simulations is reduced by the fact that the localization of the plastic strains ceases at the occurrence of fracture. At the same time, the use of fine meshes allows capturing characteristic features of ductile fracture, such as cracking along shear-bands or cup-and-cone fracture. In view of improving the numerical efficiency of the analyses, a predictor–corrector algorithm for adaptive local refinement employing LR NURBS was adopted, so that a fine mesh can be employed only in the vicinity of the crack, without the need of knowing in advance the fracture pattern.

The effectiveness of the numerical approach has been validated through the comparison with results from experimental test. We especially highlight the example featuring the indentation tests performed on steel stiffened panels for simulating the consequences of grounding on ship hulls. The material parameters for the simulations have been determined only according to the available results of tensile tests operated on specimens from the same plates used in the experiments. The qualitative (crack patterns) and quantitative (load–displacement curves) agreement of the results of the simulations and of the tests highlights the potential and the flexibility of the phase-field method also for ductile fracture, and its possible application to the prediction of the failure of real-world structures.

Declaration of competing interest

The authors declare that they have no known competing financial interests or personal relationships that could have appeared to influence the work reported in this paper.

Acknowledgments

The authors gratefully acknowledge the support from the European Research Council through the ERC Consolidator Grant *FDM*^{2}, grant number 864482, along with the support from the Research Council of Norway, NFR, and the German Academic Exchange Service, DAAD, Germany, through the project *FATIKA - Isogeometric phase-field modeling of fatigue in slender structures*, project number 281247.

§ Figs. 14 and 17 reproduced from International Journal of Impact Engineering, Vol. 36, H. S. Alsos, J. Amdahl, On the resistance to penetration of stiffened plates, Part I-Experiments, Pages 799–807, Copyright (2009), with permission from Elsevier.

References

[1] A.A. Griffith, The phenomena of rupture and flow in solids, Phil. Trans. R. Soc. A 221 (1921) 163–198.
[2] G.A. Francfort, J.-J. Marigo, Revisiting brittle fracture as an energy minimization problem, J. Mech. Phys. Solids 46 (8) (1998) 1319–1342.
[3] B. Bourdin, G.A. Francfort, J.-J. Marigo, Numerical experiments in revisited brittle fracture, J. Mech. Phys. Solids 48 (4) (2000) 797–826.
[4] H. Amor, J.-J. Marigo, C. Maurini, Regularized formulation of the variational brittle fracture with unilateral contact: Numerical experiments, J. Mech. Phys. Solids 57 (8) (2009) 1209–1229.
[5] C. Miehe, M. Hofacker, F. Welschinger, A phase field model for rate-independent crack propagation: Robust algorithmic implementation based on operator splits, Comput. Methods Appl. Mech. Engrg. 199 (45) (2010) 2765–2778.
[6] F. Freddi, G. Royer-Carfagni, Regularized variational theories of fracture: A unified approach, J. Mech. Phys. Solids 58 (8) (2010) 1154–1174.
[7] C. Steinke, M. Kaliske, A phase-field crack model based on directional stress decomposition, Comput. Mech. 63 (5) (2019) 1019–1046.
[8] C. Kuhn, A. Schlüter, R. Müller, On degradation functions in phase field fracture models, Comput. Mater. Sci. 108 (2015) 374–384.
[9] M.J. Borden, T.J.R. Hughes, C.M. Landis, A. Anvari, I.J. Lee, A phase-field formulation for fracture in ductile materials: Finite deformation balance law derivation, plastic degradation, and stress triaxiality effects, Comput. Methods Appl. Mech. Engrg. 312 (2016) 130–166.
[10] T. Gerasimov, L. De Lorenzis, A line search assisted monolithic approach for phase-field computing of brittle fracture, Comput. Methods Appl. Mech. Engrg. 312 (2016) 276–303.
[11] M.J. Borden, T.J.R. Hughes, C.M. Landis, C.V. Verhoosel, A higher-order phase-field model for brittle fracture: Formulation and analysis within the isogeometric analysis framework, Comput. Methods Appl. Mech. Engrg. 273 (2014) 100–118.
[12] K. Pham, H. Amor, J.-J. Marigo, C. Maurini, Gradient damage models and their use to approximate brittle fracture, Int. J. Damage Mech. 20 (4) (2011) 618–652.
[13] C. Miehe, M. Hofacker, L.-M. Schänzel, F. Aldakheel, Phase field modeling of fracture in multi-physics problems. Part ii. coupled brittle-to-ductile failure criteria and crack propagation in thermo-elastic-plastic solids, Comput. Methods Appl. Mech. Engrg. 294 (2015) 486–522.
[14] R. Alessi, M. Ambati, T. Gerasimov, S. Vidoli, L. De Lorenzis, Comparison of phase-field models of fracture coupled with plasticity, in: Advances in Computational Plasticity: A Book in Honour of D. Roger J. Owen, Springer International Publishing, Cham, 2018, pp. 1–21.
[15] F.P. Duda, A. Ciarbonetti, P.J. Sánchez, A.E. Huespe, A phase-field/gradient damage model for brittle fracture in elastic-plastic solids, Int. J. Plast. 65 (2015) 269–296.
[16] M. Ambati, T. Gerasimov, L. De Lorenzis, Phase-field modeling of ductile fracture, Comput. Mech. 55 (5) (2015) 1017–1040.
[17] M. Ambati, R. Kruse, L. De Lorenzis, A phase-field model for ductile fracture at finite strains and its experimental verification, Comput. Mech. 57 (1) (2016) 149–167.
[18] R. Alessi, J.-J. Marigo, S. Vidoli, Gradient damage models coupled with plasticity and nucleation of cohesive cracks, Arch. Ration. Mech. Anal. 214 (2) (2014) 575–615.
[19] R. Alessi, J.-J. Marigo, S. Vidoli, Gradient damage models coupled with plasticity: Variational formulation and main properties, Mech. Mater. 80 (2015) 351–367.
[20] C. Kuhn, T. Noll, R. Müller, On phase field modeling of ductile fracture, GAMM-Mitt. 39 (1) (2016) 35–54.
[21] C. Huang, X. Gao, Development of a phase field method for modeling brittle and ductile fracture, Comput. Mater. Sci. 169 (2019) 109089.
[22] P. Rodriguez, J. Ulloa, C. Samaniego, E. Samaniego, A variational approach to the phase field modeling of brittle and ductile fracture, Int. J. Mech. Sci. 144 (2018) 502–517.
[23] C. Miehe, S. Teichtmeister, F. Aldakheel, Phase-field modelling of ductile fracture: a variational gradient-extended plasticity-damage theory and its micromorphic regularization, Phil. Trans. R. Soc. A 374 (2066) (2016) 20150170.
[24] B. Yin, M. Kaliske, A ductile phase-field model based on degrading the fracture toughness: Theory and implementation at small strain, Comput. Methods Appl. Mech. Engrg. 366 (2020) 113068.
[25] M. Dittmann, F. Aldakheel, J. Schulte, P. Wriggers, C. Hesch, Variational phase-field formulation of non-linear ductile fracture, Comput. Methods Appl. Mech. Engrg. 342 (2018) 71–94.
[26] H. Ulmer, M. Hofacker, C. Miehe, Phase field modeling of fracture in plates and shells, Proc. Appl. Math. Mech. 12 (1) (2012) 171–172.
[27] F. Amiri, D. Millán, Y. Shen, T. Rabczuk, M. Arroyo, Phase-field modeling of fracture in linear thin shells, Theor. Appl. Fract. Mech. 69 (2014) 102–109.
[28] P. Areias, T. Rabczuk, M.A. Msekh, Phase-field analysis of finite-strain plates and shells including element subdivision, Comput. Methods Appl. Mech. Engrg. 312 (2016) 322–350.
[29] J. Reinoso, M. Paggi, C. Linder, Phase field modeling of brittle fracture for enhanced assumed strain shells at large deformations: formulation and finite element implementation, Comput. Mech. 59 (6) (2017) 981–1001.
[30] J. Kiendl, M. Ambati, L. De Lorenzis, H. Gomez, A. Reali, Phase-field description of brittle fracture in plates and shells, Comput. Methods Appl. Mech. Engrg. 312 (2016) 374–394.
[31] K. Paul, C. Zimmermann, K.K. Mandadapu, T.J.R. Hughes, C.M. Landis, R.A. Sauer, An adaptive space-time phase field formulation for dynamic fracture of brittle shells based on LR NURBS, Comput. Mech. (2020).

[32] D. Proserpio, M. Ambati, L. De Lorenzis, J. Kiendl, A framework for efficient isogeometric computations of phase-field brittle fracture in multipatch shell structures, Comput. Methods Appl. Mech. Engrg. 372 (2020) 113363.
[33] K. Paul, C. Zimmermann, T.X. Duong, R.A. Sauer, Isogeometric continuity constraints for multi-patch shells governed by fourth-order deformation and phase field models, Comput. Methods Appl. Mech. Engrg. 370 (2020) 113219.
[34] G. Kikis, M. Ambati, L. De Lorenzis, S. Klinkel, Phase-field model of brittle fracture in Reissnmoder–Mindlin plates and shells, Comput. Methods Appl. Mech. Engrg. 373 (2021) 113490.
[35] U. Pillai, S.P. Triantafyllou, I. Ashcroft, Y. Essa, F.M. de la Escalera, Phase-field modelling of brittle fracture in thin shell elements based on the MITC4+ approach, Comput. Mech. 65 (6) (2020) 1413–1432.
[36] M. Ambati, L. De Lorenzis, Phase-field modeling of brittle and ductile fracture in shells with isogeometric NURBS-based solid-shell elements, Comput. Methods Appl. Mech. Engrg. 312 (Supplement C) (2016) 351–373.
[37] M. Ambati, T. Gerasimov, L. De Lorenzis, A review on phase-field models of brittle fracture and a new fast hybrid formulation, Comput. Mech. 55 (2) (2015) 383–405.
[38] A. Mesgarnejad, B. Bourdin, M.M. Khonsari, Validation simulations for the variational approach to fracture, Comput. Methods Appl. Mech. Engrg. 290 (2015) 420–437.
[39] K.H. Pham, K. Ravi-Chandar, C.M. Landis, Experimental validation of a phase-field model for fracture, Int. J. Fract. 205 (1) (2017) 83–101.
[40] T. Wu, A. Carpiuc-Prisacari, M. Poncelet, L. De Lorenzis, Phase-field simulation of interactive mixed-mode fracture tests on cement mortar with full-field displacement boundary conditions, Eng. Fract. Mech. 182 (2017) 658–688.
[41] E. Tanné, T. Li, B. Bourdin, J.-J. Marigo, C. Maurini, Crack nucleation in variational phase-field models of brittle fracture, J. Mech. Phys. Solids 110 (2018) 80–99.
[42] D. Wick, T. Wick, R.J. Hellmig, H.-J. Christ, Numerical simulations of crack propagation in screws with phase-field modeling, Comput. Mater. Sci. 109 (2015) 367–379.
[43] J. Kiendl, K.-U. Bletzinger, J. Linhard, R. Wüchner, Isogeometric shell analysis with Kirchhoff–Love elements, Comput. Methods Appl. Mech. Engrg. 198 (49) (2009) 3902–3914.
[44] J.C. Simo, A framework for finite strain elastoplasticity based on maximum plastic dissipation and the multiplicative decomposition: Part I. Continuum formulation, Comput. Methods Appl. Mech. Engrg. 66 (2) (1988) 199–219.
[45] M. Ambati, J. Kiendl, L. De Lorenzis, Isogeometric Kirchhoff–Love shell formulation for elasto-plasticity, Comput. Methods Appl. Mech. Engrg. 340 (2018) 320–339.
[46] J. Kiendl, M.-C. Hsu, M.C.H. Wu, A. Reali, Isogeometric Kirchhoff–Love shell formulations for general hyperelastic materials, Comput. Methods Appl. Mech. Engrg. 291 (2015) 280–303.
[47] L. Ambrosio, V. Tortorelli, On the approximation of free discontinuity problems, Boll. Unione Mat. Italiana B 6 (1992) 105–123.
[48] A.J. Herrema, E.L. Johnson, D. Proserpio, M.C.H. Wu, J. Kiendl, M.-C. Hsu, Penalty coupling of non-matching isogeometric Kirchhoff–Love shell patches with application to composite wind turbine blades, Comput. Methods Appl. Mech. Engrg. 346 (2019) 810–840.
[49] R. Dimitri, L. De Lorenzis, M.A. Scott, P. Wriggers, R.L. Taylor, G. Zavarise, Isogeometric large deformation frictionless contact using T-splines, Comput. Methods Appl. Mech. Engrg. 269 (2014) 394–414.
[50] E.L. Holten, Isogeometric contact analysis: Implementation of a penalty-based algorithm, (Master's thesis), NTNU, 2019.
[51] L. Piegl, W. Tiller, The NURBS Book, Springer Science & Business Media, 2012.
[52] L. De Lorenzis, P. Wriggers, C. Weißenfels, Computational contact mechanics with the finite element method, in: Encyclopedia of Computational Mechanics Second Edition, American Cancer Society, 2017, pp. 1–45.
[53] C. Zimmermann, R.A. Sauer, Adaptive local surface refinement based on LR NURBS and its application to contact, Comput. Mech. 60 (6) (2017) 1011–1031.
[54] K.A. Johannessen, T. Kvamsdal, T. Dokken, Isogeometric analysis using LR B-splines, Comput. Methods Appl. Mech. Engrg. 269 (2014) 471–514.
[55] J. Besson, Continuum models of ductile fracture: A review, Int. J. Damage Mech. 19 (1) (2010) 3–52.
[56] J.F. Caseiro, R.A.F. Valente, A. Reali, J. Kiendl, F. Auricchio, R.J. Alves de Sousa, On the assumed natural strain method to alleviate locking in solid-shell NURBS-based finite elements, Comput. Mech. 53 (6) (2014) 1341–1353.
[57] C.M. Muscat-Fenech, A.G. Atkins, Out-of-plane stretching and tearing fracture in ductile sheet materials, Int. J. Fract. 84 (4) (1997) 297–306.
[58] P.M.A. Areias, J.H. Song, T. Belytschko, Analysis of fracture in thin shells by overlapping paired elements, Comput. Methods Appl. Mech. Engrg. 195 (41) (2006) 5343–5360.
[59] H.S. Alsos, J. Amdahl, On the resistance to penetration of stiffened plates, Part I–Experiments, Int. J. Impact Eng. 36 (6) (2009) 799–807.
[60] H.S. Alsos, J. Amdahl, O.S. Hopperstad, On the resistance to penetration of stiffened plates, part II: Numerical analysis, Int. J. Impact Eng. 36 (7) (2009) 875–887.